



Finding Quasars behind the Galactic Plane. I. Candidate Selections with Transfer Learning

Yuming Fu^{1,2} , Xue-Bing Wu^{1,2} , Qian Yang³, Anthony G. A. Brown⁴ , Xiaotong Feng^{1,2}, Qinchen Ma^{1,2}, and Shuyan Li¹

¹ Department of Astronomy, School of Physics, Peking University, Beijing 100871, People's Republic of China; fuym@pku.edu.cn, wuxb@pku.edu.cn

² Kavli Institute for Astronomy and Astrophysics, Peking University, Beijing 100871, People's Republic of China

³ Department of Astronomy, University of Illinois at Urbana-Champaign, Urbana, IL 61801, USA

⁴ Leiden Observatory, Leiden University, Niels Bohrweg 2, 2333 CA, Leiden, The Netherlands

Received 2020 September 10; revised 2021 January 30; accepted 2021 February 18; published 2021 April 23

Abstract

Quasars behind the Galactic plane (GPQs) are important astrometric references and useful probes of Milky Way gas. However, the search for GPQs is difficult due to large extinctions and high source densities in the Galactic plane. Existing selection methods for quasars developed using high Galactic latitude (high- b) data cannot be applied to the Galactic plane directly because the photometric data obtained from high- b regions and the Galactic plane follow different probability distributions. To alleviate this data set shift problem for quasar candidate selection, we adopt a transfer-learning framework at both the data and algorithm levels. At the data level, to make a training set in which a data set shift is modeled, we synthesize quasars and galaxies behind the Galactic plane based on SDSS sources and the Galactic dust map. At the algorithm level, to reduce the effect of class imbalance, we transform the three-class classification problem for stars, galaxies, and quasars into two binary classification tasks. We apply the XGBoost algorithm to Pan-STARRS1 (PS1) and AllWISE photometry for classification and an additional cut on Gaia proper motion to remove stellar contaminants. We obtain a reliable GPQ candidate catalog with 160,946 sources located at $|b| \leq 20^\circ$ in the PS1-AllWISE footprint. Photometric redshifts of GPQ candidates achieved with the XGBoost regression algorithm show that our selection method can identify quasars in a wide redshift range ($0 < z \lesssim 5$). This study extends the systematic searches for quasars to the dense stellar fields and shows the feasibility of using astronomical knowledge to improve data mining under complex conditions in the big-data era.

Unified Astronomy Thesaurus concepts: Active galactic nuclei (16); Astrostatistics techniques (1886); Classification (1907); Catalogs (205); Quasars (1319); Galactic and extragalactic astronomy (563)

Supporting material: FITS file

1. Introduction

The Galactic plane has long been the “zone of avoidance” for extragalactic astronomy, including quasar surveys. The Half Million Quasar (Flesch 2015) catalog contains a total of 510,764 objects but only 35,105 located at $b \leq |30^\circ|$ (half of the whole sky area), 3730 at $b \leq |20^\circ|$, and 255 at $b \leq |10^\circ|$. Although it is difficult to search for quasars behind the Galactic plane (GPQs), such quasars are important references for astrometry and useful probes of Milky Way gas.

Quasars are used as astrometric references due to their small parallaxes and proper motions. The GPQs enable the accurate measurement of positions, distances, and proper motions of stars in the Galactic disk, which is key to understanding our own Galaxy. The high-precision astrometry provided by the Gaia mission defines a celestial reference frame through the positions of 556,869 candidate quasars; however, only a tiny fraction of these quasars are located at $|b| \leq 15^\circ$ (Gaia Collaboration et al. 2018b). A large sample of GPQs will help build a better reference frame in the optical through direct coverage of the sky in the Galactic plane and reach a better understanding of the systematic astrometry errors of Gaia in the Galactic plane region (Arenou et al. 2018).

Line-of-sight absorption toward quasars can probe the gas structures of the Milky Way. While quasars at high Galactic latitude have been useful in studying the Milky Way halo gas (e.g., Savage et al. 1993, 2000; Ben Bekhti et al. 2008, 2012), GPQs allow absorption line studies on gaseous structures in the

Galactic plane (e.g., anticenter shell, H complex; see Westmeier 2018). Moreover, a high-density sample of GPQs can map the gas distribution with a higher angular resolution than is possible with the 21 cm surveys.

Another application of GPQs is adaptive optics observation of quasar host galaxies, which is achieved by their proximity to nearby bright stars as natural guide stars (Im et al. 2007; Fischer et al. 2019). For adaptive optics, natural guide stars should be located within a few arcseconds of the science target, which rarely occurs outside of the Galactic plane but is more common in the plane.

The difficulty of finding GPQs is caused by several challenges, including the following.

1. In comparison to objects at high Galactic latitude (high- b), sources in the Galactic plane suffer from higher extinction and reddening. As a result, many sources (especially extragalactic sources) cannot be detected within the survey detection limit. For other detectable sources, their colors are different from those at high Galactic latitude.
2. The source density in the Galactic plane is high. The quality of photometry can be worse in dense regions, because sources can be easily contaminated by visible or unseen neighbors.
3. A lot of “unusual” stars are located within the Galactic plane, including some white dwarfs, M/L/T dwarfs, and young stellar objects (YSOs), that share many similar

observational properties with quasars. These sources can be contaminants for quasars at different redshifts (e.g., Kirkpatrick et al. 1997; Vennes et al. 2002; Chiu et al. 2006; Kozłowski & Kochanek 2009).

Since the first identification of a quasar (3C 273; Schmidt 1963), many methods for quasar candidate selection have been developed, including ultraviolet excess (e.g., Sandage 1965; Green et al. 1986), radio sources (e.g., Gregg et al. 1996; White et al. 2000; Becker et al. 2001), X-ray sources (e.g., Pounds 1979; Grazian et al. 2000), optical/near-infrared (near-IR) colors (e.g., Fan et al. 2001; Richards et al. 2002; Wu & Jia 2010), mid-IR colors (e.g., Lacy et al. 2004; Stern et al. 2005, 2012; Mateos et al. 2012; Wu et al. 2012; Yan et al. 2013), and quasar variability (e.g., Dobrzański et al. 2003; Palanque-Delabrouille et al. 2011). In addition, tools based on statistical machine learning (e.g., Richards et al. 2004; Bovy et al. 2011) and deep learning (e.g., Yèche et al. 2010; Pasquet-Itam & Pasquet 2018) have also been established to find quasars with various data that are available.

A few studies have focused on finding quasars/active galactic nuclei (AGNs) behind dense stellar fields such as the Galactic plane, Magellanic Clouds, and M31 and M33 galaxies. Most of these studies used infrared selection methods to efficiently find quasars. For example, Im et al. (2007) discovered 40 bright quasars at $|b| \leq 20^\circ$ by applying the combination of a near-IR color cut of $J - K > 1.4$ on the Two Micron All Sky Survey (2MASS; Skrutskie et al. 2006) and detection of a radio counterpart from the NRAO VLA Sky Survey (Condon et al. 1998). Kozłowski & Kochanek (2009) identified 5000 AGNs behind the Magellanic Clouds with mid-IR color cuts modified from the method of Stern et al. (2005). Huo et al. (2010, 2013, 2015) discovered 1870 new quasars around the Andromeda (M31) and Triangulum (M33) galaxies with the Large Sky Area Multi-Object Fiber Spectroscopic Telescope (LAMOST) from 2009 to 2013.

Recently, searches for quasars have been focused on large data sets with big data volumes and large sky coverage. Secretst et al. (2015) obtained an all-sky AGN candidate catalog with ~ 1.4 million sources using two-color infrared photometric selection criteria from the Wide-field Infrared Survey Explorer final catalog release (AllWISE; Wright et al. 2010; Mainzer et al. 2011). Assef et al. (2018) built two catalogs of AGN candidates that were also based on AllWISE photometry while excluding regions around the Galactic center and Galactic plane. Jin et al. (2019) selected quasar candidates with the machine-learning method using Pan-STARRS1 (PS1; Chambers et al. 2016) and AllWISE data. Bailer-Jones et al. (2019) classified objects in the Gaia Data Release 2 (Gaia DR2; Gaia Collaboration et al. 2018a, 2016) as stars, quasars, and galaxies with a Gaussian mixture model and addressed the problem of class imbalance in Gaia DR2.

However, the studies listed above either treated sources in the Galactic plane and high Galactic latitude as the same or removed the Galactic plane from consideration. Selection methods for quasars at high Galactic latitude are not generic and cannot be applied to the Galactic plane directly because data (e.g., PS1 and AllWISE photometry) obtained from high- and low- b follow different probability distributions. For example, the apparent colors of quasars (stars) vary from high- to low- b regions, and so does the source density of quasars (stars). Such behavior of the data is a kind of nonstationarity called *data set shift* (Quionero-Candela et al. 2009), which

leads to a significant estimation bias of supervised machine-learning algorithms. The color cuts for quasar selection can also be regarded as simple decision tree models in a machine-learning regime. Previous color cuts obtained from high Galactic latitude regions fail in the Galactic plane due to the data set shift.

To deal with these data set shift problems, *transfer learning* (Pan & Yang 2009) has been proposed and studied extensively by data scientists. The idea of transfer learning is to use knowledge gained in one problem and apply it to a different but related problem. Although spectroscopically identified (i.e., “labeled”) samples of extragalactic objects are inadequate in the Galactic plane, such labeled samples are available at high Galactic latitude. The labeled data make it possible to build a good selection method for GPQs once the knowledge transfer from high Galactic latitude to low Galactic latitude is successful.

This paper is the first of a series for finding GPQs. In this paper, we present a transfer-learning method for quasar selection, as well as a GPQ candidate catalog with 160,946 sources. In Section 2, we introduce the archival data used for this study. In Section 3, we describe the algorithm design for GPQ selection. In Section 4, we synthesize quasars and galaxies behind the Galactic plane with extragalactic objects at high Galactic latitude from the Sloan Digital Sky Survey (SDSS; York et al. 2000) to make a training set in which the data set shift is modeled. In Section 5, we transform the three-class classification problem for stars, galaxies, and quasars to two binary classification tasks, stars versus extragalactic objects and quasars versus galaxies, to reduce the class imbalance and class-balance change. In Section 6, we calculate the photometric redshifts for GPQ candidates. In Section 7, we present the GPQ candidate catalog and some statistical properties of the sample. We summarize the results in Section 8. Throughout this paper, we use AB magnitude for PS1 photometry and Vega magnitude for AllWISE photometry unless otherwise mentioned.

2. Data

We make use of optical and infrared photometric data from PS1 and AllWISE and astrometric data from Gaia DR2. We also retrieve samples of spectroscopically identified objects from SDSS and LAMOST.

2.1. PS1 DR1 Photometry

A set of synoptic imaging sky surveys was carried out by PS1 (Chambers et al. 2016), including the 3π Steradian Survey and the Medium Deep Survey in five bands ($grizy_{P1}$). The mean 5σ point-source limiting sensitivities in the stacked 3π Steradian Survey in ($grizy_{P1}$) are (23.3, 23.2, 23.1, 22.3, 21.4), and the single-epoch 5σ depths in ($grizy_{P1}$) are (22.0, 21.8, 21.5, 20.9, 19.7). For better astrometry in the crowded Galactic plane field, we use mean coordinates from the PS1 MeanObject table. Mean point-spread function (PSF) magnitudes are used for all bands ($grizy_{P1}$), and mean Kron magnitudes (Kron 1980) are used for the i_{P1} and z_{P1} bands. The Galactic extinction coefficients for ($grizy_{P1}$) are $R_g, R_r, R_i, R_z, R_y = 3.5805, 2.6133, 1.9468, 1.5097, 1.2245$. These coefficients are calculated using $R_\lambda = A_\lambda/A_V \times R_V$, where A_λ/A_V is the relative extinction value for band λ given by a new optical to mid-IR extinction law (Wang & Chen 2019), and $R_V = 3.1$.

We set a few constraints on the PS1 data to ensure data quality. All sources should be (i) detected in all PS1 bands ($grizy_{P1} > 0$) and significantly detected in i_{P1} (error in PSF mag of i_{P1} band $i_{err} < 0.2171$, equivalent to i_{P1} -band signal-to-noise ratio (S/N) larger than 5), (ii) not too bright in i_{P1} to avoid possible saturation ($i > 14$), and (iii) measured with Kron magnitude (Kron 1980) in the i_{P1} and z_{P1} bands ($i_{\text{Kron}} > 0$ and $z_{\text{Kron}} > 0$). For simplification, we use (g, r, i, z, y) to represent the PSF magnitudes of the PS1 bands ($grizy_{P1}$) in color indexes (e.g., $g - r$, $g - W1$) and derived quantities $i - i_{\text{Kron}}$ and $z - z_{\text{Kron}}$. The z_{P1} PSF magnitude does not appear alone and will not be confused with the redshift symbol z .

2.2. AllWISE Photometry for Pointlike Sources

The AllWISE catalog is built upon the work of the Wide-field Infrared Survey Explorer (WISE) mission (Wright et al. 2010) by combining data from the WISE cryogenic and NEOWISE (Mainzer et al. 2011) postcryogenic surveys. WISE has four bands at 3.4, 4.6, 12, and 22 μm (W1, W2, W3, and W4). The 5 σ limiting magnitudes of the AllWISE catalog in the W1, W2, W3, and W4 bands are 19.6, 19.3, 16.7, and 14.6 mag. The Galactic extinction coefficients for W1, W2, and W3 used in this study are $R_{W1}, R_{W2}, R_{W3} = 0.1209, 0.0806, 0.124$. These coefficients are also calculated with relative extinction A_{λ}/A_V values from Wang & Chen (2019).

We cross-match the PS1 sources with AllWISE using a radius of 1'' to avoid source confusion in the dense fields of the Galactic plane. We also set a few constraints on the AllWISE data. All sources should be (i) AllWISE point sources ($ext_flg = 0$), (ii) not too bright to avoid possible saturation ($W1 > 8$ and $W2 > 7$), (iii) significantly detected in the W1 and W2 bands ($W1_{snr} > 5$ and $W2_{snr} > 5$, where $W1_{snr}/W2_{snr}$ means the S/N in the W1/W2 band), (iv) unaffected by prioritized image artifacts in each band ($cc_flags = "0000"$), and (v) unblended with nearby detections so that only one component is used in each profile fitting for each source ($nb = 1$).

2.3. Gaia DR2 Astrometry

Gaia DR2 (Gaia Collaboration et al. 2018a, 2016) contains celestial positions and the apparent brightness in the G band for approximately 1.7 billion sources. For 1.3 billion of those sources, parallaxes and proper motions are available. Broad-band photometry in the G_{BP} (330–680 nm) and G_{RP} (630–1050 nm) bands are available for 1.4 billion sources. We use the proper motions and their uncertainties from the Gaia DR2 catalog (columns pmra , pmra_error , pmdec , and pmdec_error) to find quasars.

2.4. SDSS Quasar Catalog: The 14th Data Release

The SDSS (York et al. 2000) has mapped the high Galactic latitude northern sky and obtained imaging as well as spectroscopy data for millions of objects, including stars, galaxies, and quasars. The 14th data release of the SDSS Quasar Catalog (SDSS DR14Q; Pâris et al. 2018) contains 526,356 quasars. We cross-match the DR14Q catalog with PS1 and AllWISE, both with a radius of 1''. To ensure the data quality, we use the same constraints in Sections 2.1 and 2.2 to retrieve a subset of DR14Q. This subset has 289,271 sources and is denoted as GoodQSO hereafter. As can be seen from the HEALPix (Górski et al. 2005) density map of GoodQSO

(Figure 1), very few sources of GoodQSO are located at $|b| \leqslant 20^\circ$.

2.5. SDSS Spectroscopically Identified Stars and Galaxies

In order to compare the high- b sources with the Galactic plane sources that we use, samples of stars and galaxies are extracted from the SpecPhotoAll table of SDSS Data Release 15 (Blanton et al. 2017; Aguado et al. 2019). We cross-match both the star and galaxy samples with PS1 and AllWISE with a radius of 1''. The SDSS star sample has 23,693 sources. We also apply quality constraints in Sections 2.1 and 2.2 to select galaxy subsets with good photometry for later use. The resulting subset of galaxies (denoted as GoodGal hereafter) has 1,635,053 sources. Most SDSS stars and galaxies are located at high Galactic latitude ($|b| > 20^\circ$).

2.6. Stars from LAMOST General Catalog

LAMOST, also called the Guoshoujing Telescope, is a special reflecting Schmidt telescope, the design of which allows both a large effective aperture of 3.6–4.9 m and a wide field of view of 5° (Wang et al. 1996; Su & Cui 2004; Cui et al. 2012). The LAMOST spectral survey (Luo et al. 2012, 2015; Zhao et al. 2012) consists of two major components, i.e., the LAMOST Experiment for Galactic Understanding and Exploration (LEGUE; Deng et al. 2012) and the LAMOST ExtraGalactic Survey (LEGAS). The LEGUE observes stars in different sky regions with different magnitude ranges, including the Galactic halo with $r < 16.8$ mag at $|b| > 30^\circ$, the Galactic anticenter with 14.0 mag $< r < 17.8$ mag at $150^\circ \leq l \leq 210^\circ$ and $|b| < 30^\circ$ (Yuan et al. 2015), and the Galactic disk with $r \lesssim 16$ mag at $|b| \leqslant 20^\circ$ with uniform coverage along the Galactic longitude. The LEGAS mainly identifies galaxies and quasars that are within the SDSS footprint but complementary to the SDSS spectroscopic samples (e.g., Shen et al. 2016; Yao et al. 2019). Nevertheless, extragalactic objects in the LEGUE plates are also targets of the LEGAS. The LAMOST spectral survey has obtained the largest stellar spectra sample to date. We retrieve a star sample from the LAMOST general catalog from DR1 to DR7v0. A total of 3,940,076 LAMOST stars meet the same constraints in Sections 2.1 and 2.2. From this LAMOST star sample, we select 1,334,577 Galactic plane stars with $|b| \leqslant 20^\circ$ (denoted as T_{Star} hereafter). Most T_{Star} sources are from the LEGUE survey and are brighter than 18 mag in the i_{P1} band.

2.7. The Million Quasars (Milliquas) Catalog

The Million Quasars (Milliquas) Catalog (Flesch 2019) is a compilation of quasars and quasar candidates from the literature. The Milliquas v6.4c update includes 758,908 type I QSOs and AGNs up to 2019 December 31. We use this catalog to extract an extant GPQ sample within the PS1 footprint. There are 4344 quasars located at $|b| \leqslant 20^\circ$, which are labeled as “Q” in Milliquas v6.4c. Cross-matching these 4344 known GPQs with PS1 and AllWISE, both with a radius of 1'', gives 2757 sources. After applying the same constraints as in Sections 2.1 and 2.2, we get a subset of 1853 sources. This Galactic plane subset of Milliquas quasars, denoted as MLQSUB, will be used later for candidate validation.

Table 1
Comparison of the Two Domains of Learning

Domains of Learning	Location	Labels of Stars	Labels of Quasars/Galaxies	Internal Class-balance Change
Source domain	$ b > 20^\circ$	Available	Available	Moderate
Target domain	$ b \leq 20^\circ$	Available	Unavailable	Severe

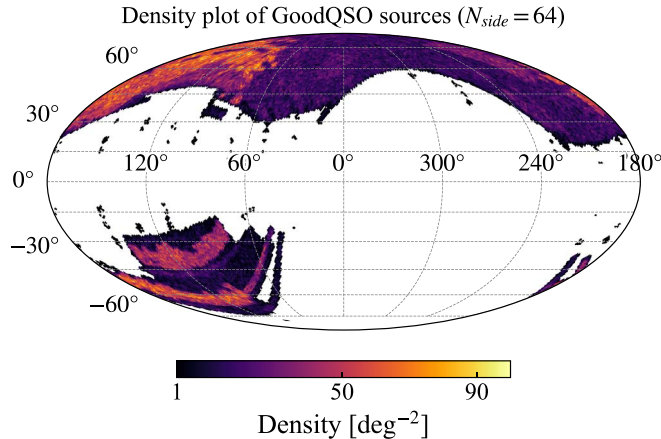


Figure 1. HEALPix density map of GoodQSO sources from SDSS DR14Q (in Galactic coordinate system) with a median density of 20.3 deg^{-2} . The HEALPix parameter $N_{\text{side}} = 64$, and the sky area per pixel is 0.839 deg^2 .

3. Design of the Transfer-learning Framework

3.1. Data Set Shift Problem in the Galactic Plane

The task of quasar selection can be described by classification problems in machine learning. Here we look into the three-class classification for stars, galaxies, and quasars with photometric data. The learning process requires two independent data sets for model training and validation. Training and validation sets can be two nonoverlapping subsets from a common parent sample with both features (colors and/or magnitudes) and class labels (star, galaxy, and quasar). Usually, the class labels are given by spectroscopic identifications. The classification algorithm learns a mapping relation from features to class labels with the training set. Often, the trained classification model (classifier) is applied to another data set without class labels (i.e., no spectroscopic identifications), which is called the application set or test set. The classifier takes features from the test set as inputs X (aka covariates) and gives class labels as outputs Y .

A basic assumption for traditional machine learning is that training and test data follow the same probability distribution (Bishop 2006; Hastie et al. 2009; Vapnik 2013). However, this assumption no longer holds if we use high- b data for model training and low- b data for application because the joint distribution of inputs and outputs $P(X, Y)$ differs between training and test data (i.e., data set shift; Quionero-Candela et al. 2009).

For our GPQ selections, the data set shift includes changes in both source colors and prior probabilities of different classes. Sources in the Galactic plane become fainter and redder than those at high Galactic latitude due to greater reddening, which changes the distribution of input features and the conditional probability of the output labels given the inputs $P(Y|X)$ (i.e., covariate shift; Shimodaira 2000; Sugiyama & Kawanabe 2012). The prior probabilities of stars are much higher than

those of quasars (and galaxies) in the Galactic plane, which means the marginal probability $P(Y)$ differs from that at high Galactic latitude (i.e., class-balance change; Saerens et al. 2002; Du Plessis & Sugiyama 2014). Moreover, the class ratio between extragalactic objects and stars may vary significantly from one place to another in the Galactic plane, which we refer to as an “internal” class-balance change of the test data.

Transfer learning can be applied to improve the learning performance under a data set shift from a source domain to the target domain (see a review in Pan & Yang 2009), where *domain* is a set \mathcal{D} that consists of a feature space \mathcal{X} and a marginal probability distribution $P(X)$, $\mathcal{D} = \{\mathcal{X}, P(X)\}$. For our classification task, the source domain data are from high Galactic latitude ($|b| > 20^\circ$), and the target domain data are from the Galactic plane ($|b| \leq 20^\circ$). In this study, we only care about areas at $\delta > -30^\circ$ due to the limits of PS1 survey coverage. Comparisons of some properties of the source and target domains are listed in Table 1.

As large numbers of stars, quasars, and galaxies have been spectroscopically identified at $|b| > 20^\circ$, labels for these three classes are available in the source domain. Since spectroscopically identified samples of quasars and galaxies are significantly lacking at $|b| \leq 20^\circ$, labels for these two classes are unavailable in the target domain. Nevertheless, the labels of many stars in the target domain are available with the help of the LAMOST spectroscopic survey.

According to the classification scheme for different settings of transfer learning by Pan & Yang (2009), the setup of classification in the Galactic plane can be categorized into transductive transfer learning, where source domain labels are available and target domain labels are unavailable. A popular approach to transductive transfer learning is feature-based transfer (e.g., Argyriou et al. 2006; Blitzer et al. 2006), which reduces the difference between the source and target domain through feature transformation in either one or both of the domains.

To solve the data set shift problem of classification in the Galactic plane, we borrow the idea of feature-based transfer learning. Using the mapping relation between the features of high- b and low- b objects, we can generate mock samples of quasars and galaxies in the Galactic plane to simulate the covariate change of their colors and magnitudes. The LAMOST Galactic plane stars also contribute to a more accurate probability distribution of data in the target domain. To reduce the effect of class-balance change, we manually go through two binary classification steps rather than running a three-class classification algorithm only once.

3.2. Modeling Covariate Change with Mock Samples

As the data of the LAMOST Galactic plane stars are available, we only focus on reducing the differences in features of extragalactic objects between training and test data. For our classification problem, all features will be constructed with photometric data from PS1 and AllWISE. We assume that the differences in photometric properties between extragalactic

objects in the Galactic plane and those off the plane are only caused by different extinctions/reddening along their sight lines. In this way, we can simply generate mock extragalactic objects behind the Galactic plane with data obtained at high Galactic latitude using the mapping relation determined by the Galactic extinction law and dust map.

The covariate change can then be shown as a color change of the extragalactic objects on a set of color–color diagrams. Our classification will perform better by adding mock samples of quasars and galaxies behind the Galactic plane into the training set.

3.3. Dealing with Class Imbalance and Class-balance Change in Machine Learning

With the data-level improvements above, the covariate change can be reduced. Efforts on the algorithm level are required to handle the class imbalance and class-balance change. During the GPQ selections, instead of performing a star–quasar binary classification, we additionally take galaxies into account and perform a three-class classification.

Many machine-learning software packages support multi-class classification jobs by transforming the task into multiple binary classification problems. However, the built-in treatment is often inflexible and sometimes destructive when dealing with class-imbalance problems. For example, in the scenario of using a one-versus-rest (also known as one-versus-all) strategy for multiclass classification, at some stages, samples of one class are regarded as the positive samples, while all samples of other classes are regarded as negative samples. Even if all of the classes in the training set have a same sample size, the binary classification situation is imbalanced, as the positive class (the “one”) has less samples than the negative class (the “rest”). In our case, the GPQ set (in both training and test set) has significantly fewer samples than the sets of galaxies and stars; thus, severe class imbalance will happen.

To reduce the disadvantage of the one-versus-rest strategy, which is commonly used in machine-learning algorithms, we manually convert this three-class classification problem into two binary classification problems. In the first step, the Galactic plane sources are classified into two classes: stars and extragalactic objects. Extragalactic objects are then classified into quasars and galaxies in the second step. By combining the two minority classes of quasar and galaxy into one, we would expect the class imbalance to be better controlled in the first step. The physical basis for merging the quasar and galaxy classes is that quasars are a special type of galaxy. For the second step, we expect the quasar-to-galaxy ratio to be nearly constant across different locations in the Galactic plane. Thus, the variable quasar-to-star or galaxy-to-star ratio is avoided, and the internal class-balance change is lessened in the learning process.

4. Mock Catalogs for Quasars and Galaxies behind the Galactic Plane

In order to construct training samples for extragalactic objects, as well as understand their covariate shift from high Galactic latitude to the Galactic plane, we synthesize quasars and galaxies behind the Galactic plane using GoodQSO and GoodGal samples. The synthesis is plausible if we assume the distribution of quasars on the celestial sphere is homogeneous and isotropic on a large scale, just as the cosmological principle

has suggested. We not only observe the changes in colors of quasars and galaxies as they are placed in low Galactic latitudes in this modeling process, but we also get a rough estimation on the sky distributions of the sources that could be detected by a certain sky survey.

4.1. Synthesizing Procedures

Let E be a set of extragalactic objects (E can be GoodQSO or GoodGal). The synthesis process consists of the following steps.

1. *Correcting for extinctions.* Extinctions of objects in set E are corrected according to a two-dimensional dust map provided by Planck Collaboration et al. (2014, hereafter [Planck14](#)) and the optical to mid-IR extinction law from Wang & Chen (2019) with $R_V = 3.1$. The $E(B - V)$ values are retrieved using a Python module, `dustmaps` (Green 2018).
2. *Assigning new locations.* We generate a random sample of points that are uniformly distributed on the sky with $|b| \leq 20^\circ$. The number of these random points is equal to the sample size of E . The coordinates of these points are randomly assigned to objects of E as their new locations. Now we get a new set, E_m (MockGPQ, MockGal), without line-of-sight extinctions.
3. *Adding new extinctions.* We add extinctions to the E_m sample using the [Planck14](#) dust map based on their new (mock) locations.
4. *Setting limiting magnitudes.* We obtain a subset of E_m by choosing sources brighter than the PS1 single-epoch 5σ depths in all PS1 passbands: $(grizy_{P1}) < (22.0, 21.8, 21.5, 20.9, 19.7)$. This subset, denoted as E_{gm} (Good-MockGPQ, GoodMockGal), represents a “good” mock sample that can be detected by the PS1 survey in all bands. However, we do not apply similar constraints to the AllWISE bands, as the magnitude that corresponds to a 5σ sensitivity varies with location. Also, this extinction selection effect relies more on the optical survey depth than the IR survey depth. Factors such as observation strategies and source confusions in dense fields are not taken into consideration in this step. Therefore, we may overestimate the detection rate of GPQs (and galaxies) through this synthesis. We select sources within the PS1 footprint (i.e., $\delta \geq -30^\circ$) and obtain the set E_{gm-PS1} (GoodMockGPQ-PS1, GoodMockGal-PS1).
5. *Constructing training sets with mock and real data.* For mock quasars that are not included in GoodMockGPQ-PS1, their original counterparts (high- b quasars in the input set GoodQSO; denoted as C_{QSO}) are also added to the training and validation sets along with Good-MockGPQ-PS1. For mock galaxies that are not included in GoodMockGal-PS1, 25% of their original counterparts (high- b galaxies in the input set GoodGal; denoted as C_{Gal}) are added to the training and validation sets. The resulting quasar and galaxy samples for training and validation are denoted as T_{QSO} and T_{Gal} , respectively; T_{QSO} , T_{Gal} , and the LAMOST Galactic plane star sample T_{Star} form the training and validation sets for machine-learning classification.

By adding good mock samples and real data (C_{QSO} and C_{Gal}) together instead of using only good mock samples as training data for quasars or galaxies, we increase the data diversity, as

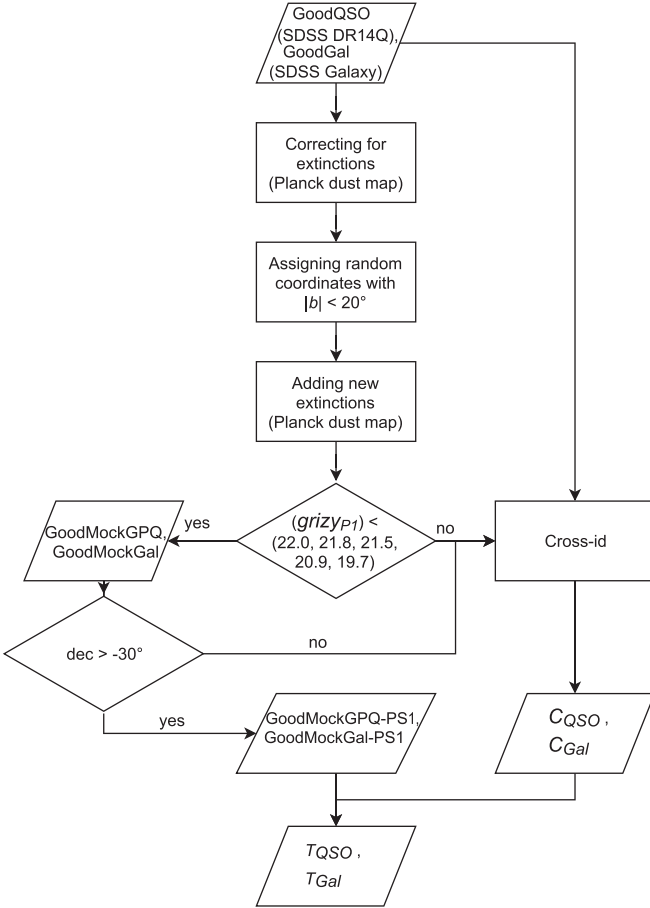


Figure 2. Flowchart of synthesizing procedures for the mock catalogs.

well as the sample size of the training set. This data diversification ensures that the training set can provide more discriminative information for the machine-learning model (Gong et al. 2019). In addition, more training data can help reduce overfitting.

The flowchart of the synthesizing procedures is displayed in Figure 2.

In the synthesizing process, we adopt the Planck14 dust map because it detects dust at a greater depth and better estimates the two-dimensional extinctions in the Galactic plane than do the dust maps constructed with stellar photometry (e.g., Green et al. 2018, 2019). We assume a uniform $R_V = 3.1$, although R_V varies slightly in the Galaxy with a dispersion of about 0.18 (Schlafly et al. 2016). Such minor variations in R_V can lead to small uncertainties of magnitudes and colors of individual mock quasars (galaxies) but have limited impacts on the statistical properties of the training sample because mock sources with large extinctions (and thus large uncertainties caused by R_V variations) are removed by the magnitude limits, as we shall see in Section 4.2.

4.2. Synthesizing Results and Data Set Shift

We define the extinction-based selection rate in the Galactic plane as $R = |E_{gm}|/|E|$, where $|E|$ is the cardinality, i.e., number of elements/sources of set E . The source numbers of the input samples are $|GoodQSO| = 289,271$ and $|GoodGal| = 1,635,053$; the source numbers of the output samples are $|GoodMockGPQ| = 101,482$ and $|GoodMockGal| = 771,392$.

Therefore, the selection rates for GPQs and galaxies are $R_{GPQ} = |GoodMockGPQ|/|GoodQSO| = 0.35$ and $R_{Gal} = |GoodMockGal|/|GoodGal| = 0.47$, respectively. The selection rate of galaxies is higher than that of GPQs because the input galaxies are, on average, brighter than the input quasars. With step 2 in Section 4.1, the sources of MockGPQ and MockGal are randomly and evenly distributed in the Galactic plane ($|b| < 20^\circ$). But after step 4, the densities of remaining sources (GoodMockGPQ and GoodMockGal) are inversely related to the dust map (Figure 3); more extragalactic sources remain detectable in regions with smaller $E(B - V)$, and voids of detection are present at regions with large $E(B - V)$. A sky survey deeper than PS1 might help make up some fraction of the gap in the middle of the Galactic plane. The GoodMockGPQ sample is sparser compared to GoodMockGal, simply because there are fewer input quasars than galaxies. Most sources of GoodMockGPQ and GoodMockGal have a line-of-sight color excess of $E(B - V) < 1.5$, which corresponds to an extinction of $A_V < 4.65$ with $R_V = 3.1$. The medians of the line-of-sight $E(B - V)$ of GoodMockGPQ-PS1 and GoodQSO are 0.21 and 0.03, respectively. In general, the GoodMockGPQ-PS1 sample has a significantly larger $E(B - V)$ compared to GoodQSO (see Figure 4(a)). Therefore, the covariate change for color indexes from high- b to low- b regions cannot be ignored. In addition, GoodMockGPQ-PS1 sources are fainter than GoodQSO sources (Figure 4(b)).

A series of color–color diagrams for GoodQSO and GoodMockGPQ-PS1, along with SDSS stars and Galactic plane point sources, are shown in Figures 5 and 6. In Figure 5, from the left to the middle panels, the covariate change of colors of quasars from high Galactic latitude to the Galactic plane can be directly observed. The Galactic reddening makes the cluster of GPQs in a color–color plane extend toward redder colors (to the upper right along the reddening vector) and scatter more than high- b quasars. The scattering is greater in color indexes of bluer bands and less at redder bands. This trend is also observable in the quasar evolutionary tracks with $E(B - V) = 0, 0.75$, and 1.5 . From the top to the bottom panels in Figure 5, the distance between two quasar evolutionary tracks with different reddening decreases.

The covariate change of stellar colors is also evident from the color–color diagrams. The stellar loci are simple and clear for high- b (SDSS) stars (see Figures 5(1a)–(3a)). However, additional spikes along the direction of increasing $E(B - V)$ appear in the stellar loci of Galactic plane stars due to reddening, as can be seen from Figures 5(1b), (1c), (2b), and (2c). Therefore, we expect to better distinguish stars from other sources using Galactic plane stars from LAMOST instead of high- b SDSS stars in the training set.

Since the mid-IR bands are less sensitive to extinction and reddening, the covariate change of AllWISE colors is less obvious than that of PS1 colors. For instance, in Figure 6(a), the quasar evolutionary tracks with $E(B - V) = 0, 0.75$, and 1.5 stay very close to each other. Since the AllWISE colors of quasars do not change much from high Galactic latitude to the Galactic plane, we can use the W1 – W2 versus W2 – W3 color–color diagram to examine the purity of the final quasar candidates by comparing the probability distributions of the candidates and GoodMockGPQ-PS1 sources.

The AllWISE color–color diagram also gives “hardness” information on the classification problem that separating quasars from galaxies is harder than separating quasars from

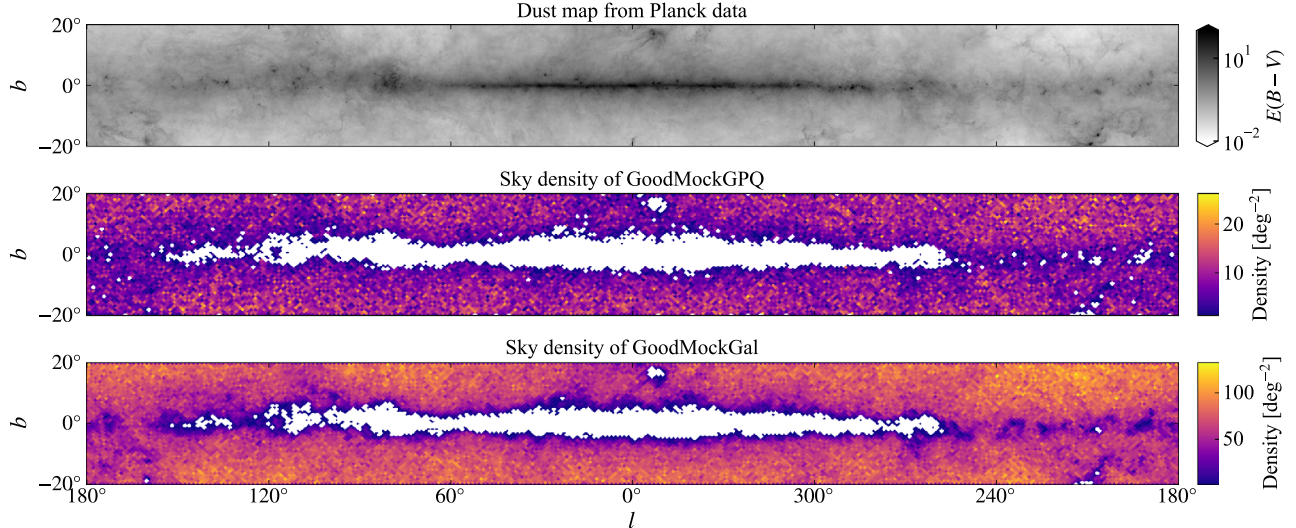


Figure 3. Dust extinction map along the Galactic plane retrieved from Planck14 (top panel) and the sky density of GoodMockGPQ (middle panel) and GoodMockGal (bottom panel).

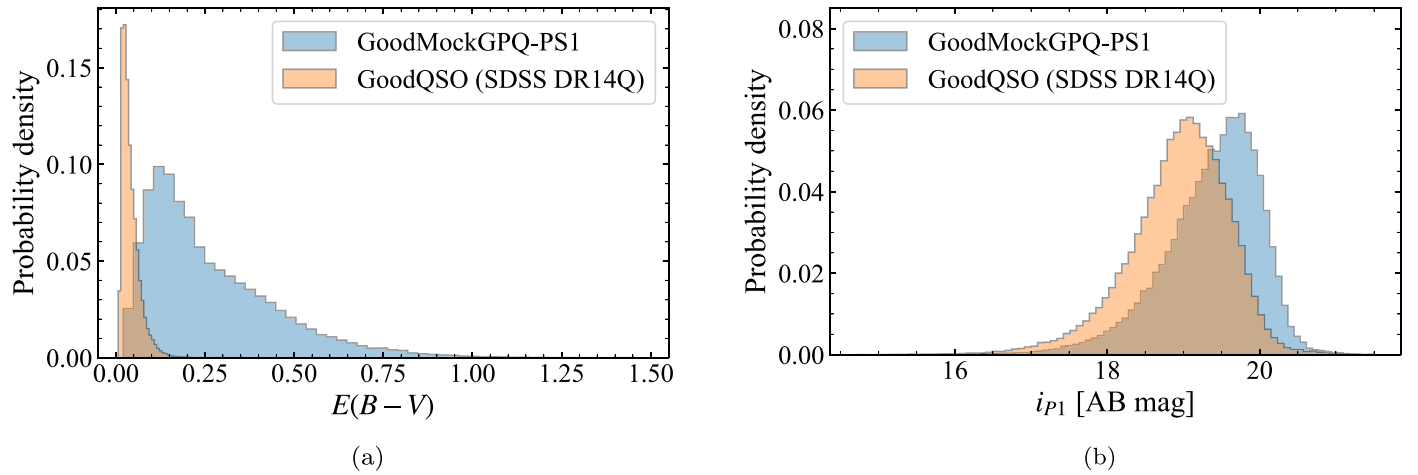


Figure 4. Histograms of (a) line-of-sight $E(B - V)$ and (b) i_{P1} -band magnitudes of GoodMockGPQ-PS1 and GoodQSO. The i_{P1} -band magnitudes are not corrected for extinction.

stars. In general, quasars have redder $W_1 - W_2$ and $W_2 - W_3$ colors than stars and galaxies due to the power-law spectral energy distributions (SEDs) and hot dust of quasars. From Figure 6(b), we can recognize the stellar locus ($W_1 - W_2 \approx 0$; lower left) and galaxy locus ($W_1 - W_2 \approx 0.5$, $W_2 - W_3 \approx 3.5$; middle right) from the density plot. The quasar reference contour line marks a “quasar region” where most quasars are located in the $W_1 - W_2$ versus $W_2 - W_3$ diagram. Most stars are away from the quasar region, while a large number of galaxies enter the quasar region, indicating that such galaxies can contaminate the mid-IR quasar selection.

Some comparisons between mock quasars (GoodMockGPQ-PS1) and mock galaxies (GoodMockGal-PS1) behind the Galactic plane are also shown in Figure 7. In the color–color diagrams of PS1 bands, galaxies largely overlap with quasars (Figures 7(a)–(c)), while on the $W_1 - W_2$ versus $W_2 - W_3$ plane, these two classes are slightly more separable (Figure 7(d)). Except for the colors, the difference between PSF magnitude and Kron (1980) magnitude is often used as a morphological separator (Strauss et al. 2002; Farrow et al. 2014) for galaxies

and point sources including quasars. However, separating quasars from galaxies becomes harder with $i_{\text{PSF}} - i_{\text{Kron}}$ at the faint end (Figure 7(e)), as has been pointed out by Yang et al. (2017). Among all ~ 1.6 million GoodGal sources, ~ 200 are point sources with $i_{\text{PSF}} < 18$ and $i_{\text{PSF}} - i_{\text{Kron}} < 0$, which can also be seen from Figure 7(e). These point sources include few quasars with “galaxy” labels and may also include some stars that are misclassified as galaxies. We do not pay attention to these point sources because they only contribute to a tiny fraction of the whole galaxy sample.

To sum up, we examine the properties of GoodMockGPQ, GoodMockGal, and PS1-AllWISE pointlike sources in the color–color spaces. For quasar candidate selection, contamination from both stars and galaxies should be taken care of. Simple PS1 color cuts are only capable of selecting quasars that are away from the stellar loci. Using a series of PS1 colors in high-dimensional space might help reduce the overlap between the stellar loci and clusters of the quasar and galaxy. Moreover, with AllWISE colors, quasars can be better separated from stars and galaxies. Therefore, we expect that

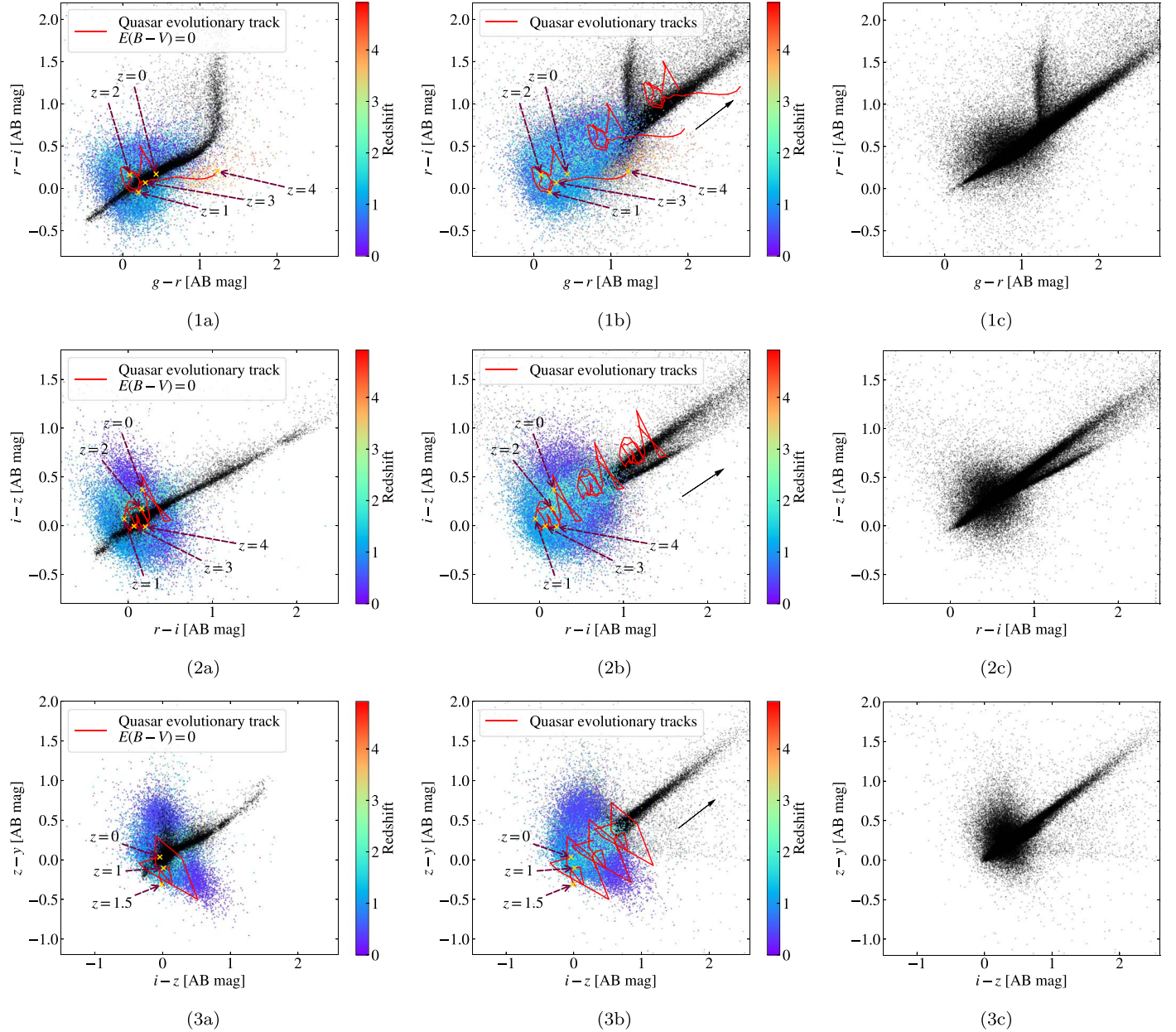


Figure 5. Color–color diagrams of (1a)–(3a) reddening-corrected GoodQSO (color-coded dots) and SDSS stars (black dots), (1b)–(3b) GoodMockGPQ-PS1 (color-coded dots) and a random sample of PS1-AllWISE point sources (black dots) in the Galactic plane ($|b| \leq 20^\circ$), and (1c)–(3c) the same sample of PS1-AllWISE point sources in the Galactic plane. For panels (1a)–(3a), quasar evolutionary tracks from redshift zero to 4 without Galactic reddening ($E(B - V) = 0$) are shown in red. For panels (1b)–(3b), quasar evolutionary tracks from redshift zero to 4 with $E(B - V) = 0, 0.75$, and 1.5 are displayed. The black arrows (reddening vectors) indicate the evolution directions of the source colors with increasing $E(B - V)$. Yellow crosses denote points on the quasar evolutionary tracks without Galactic reddening with $z = 0, 1, 2, 3$, and 4 in panels (1b) and (2b) and $z = 0, 1$, and 1.5 in panel (3b). The quasar evolutionary tracks are calculated using the optical composite quasar spectrum from Vandenberg et al. (2001) and the near-IR composite quasar spectrum from Glikman et al. (2006).

the combination of PS1 and AllWISE data will make quasar selection more efficient.

4.3. A Rough Estimation of the Lower Limit to the Sky Density of GPQs

An estimation of the sky density of GPQs will be useful for evaluating the final GPQ candidate sample and the selection method. However, the GoodMockGPQ sky distribution in the middle panel of Figure 3 does not reflect the true density of GPQs for two reasons: (i) the synthesizing process does not consider the source crowdedness and its effects on the

photometric data quality, and (ii) the source number of GoodMockGPQ only depends on the size of the input GoodQSO sample when the dust extinction map is fixed.

Let the density of GoodMockGPQ be D_{old} , then the relative density of quasars with good photometry across the Galactic plane is

$$D'_{\text{new}} = D_{\text{old}} \times \frac{D_{\text{goodph}}}{D_{\text{all}}}, \quad (1)$$

where D_{all} is the sky density of all PS1-AllWISE sources in the Galactic plane, and D_{goodph} is the sky density of sources with

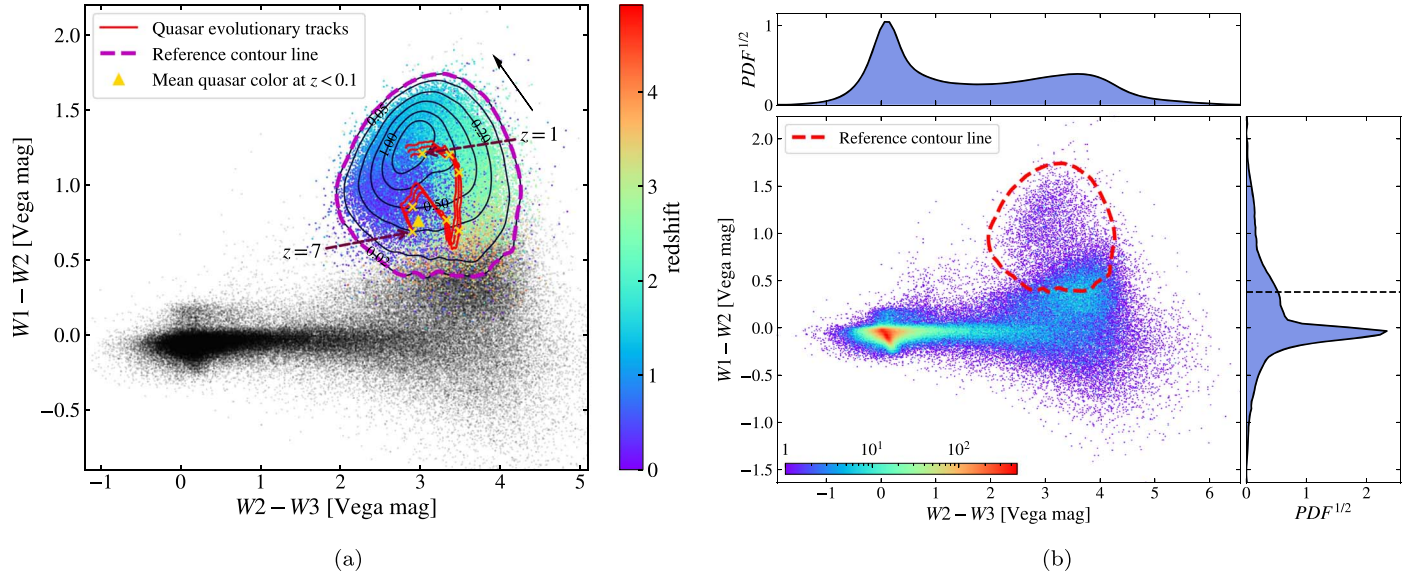


Figure 6. (a) The $W_1 - W_2$ vs. $W_2 - W_3$ color–color diagram of GoodMockGPQ-PS1 (color-coded dots) and PS1-AllWISE point sources (black dots) in the Galactic plane ($|b| \leq 20^\circ$). (b) The $W_1 - W_2$ vs. $W_2 - W_3$ color–color diagram of PS1-AllWISE point sources in the Galactic plane (color-coded according to density) and marginal probability distribution plots in the $W_1 - W_2$ and $W_2 - W_3$ axes. For panel (a), contour lines from the (two-dimensional) kernel density estimation for the GoodMockGPQ-PS1 sample are plotted, and a reference contour line (magenta) with a density of 0.02 is specified. Quasar evolutionary tracks that begin at $z = 0.6$ (due to the template coverage) and end at $z = 7$ with $E(B - V) = 0, 0.75$, and 1.5 are displayed. The black arrow (reddening vector) indicates the evolution direction of the source colors with increasing $E(B - V)$. Yellow crosses denote points on the quasar evolutionary tracks without Galactic reddening with $z = 1, \dots, 7$. The mean color of quasars with $z < 0.1$ is marked with a yellow triangle. For panel (b), the same reference contour line of the GoodMockGPQ-PS1 sample from panel (a) is shown with a red dashed line; the lowest $W_1 - W_2$ value of the reference contour line is plotted as a black dashed line over the $W_1 - W_2$ marginal distribution plot. The quasar evolutionary tracks are calculated based on the template from Hernán-Caballero et al. (2016).

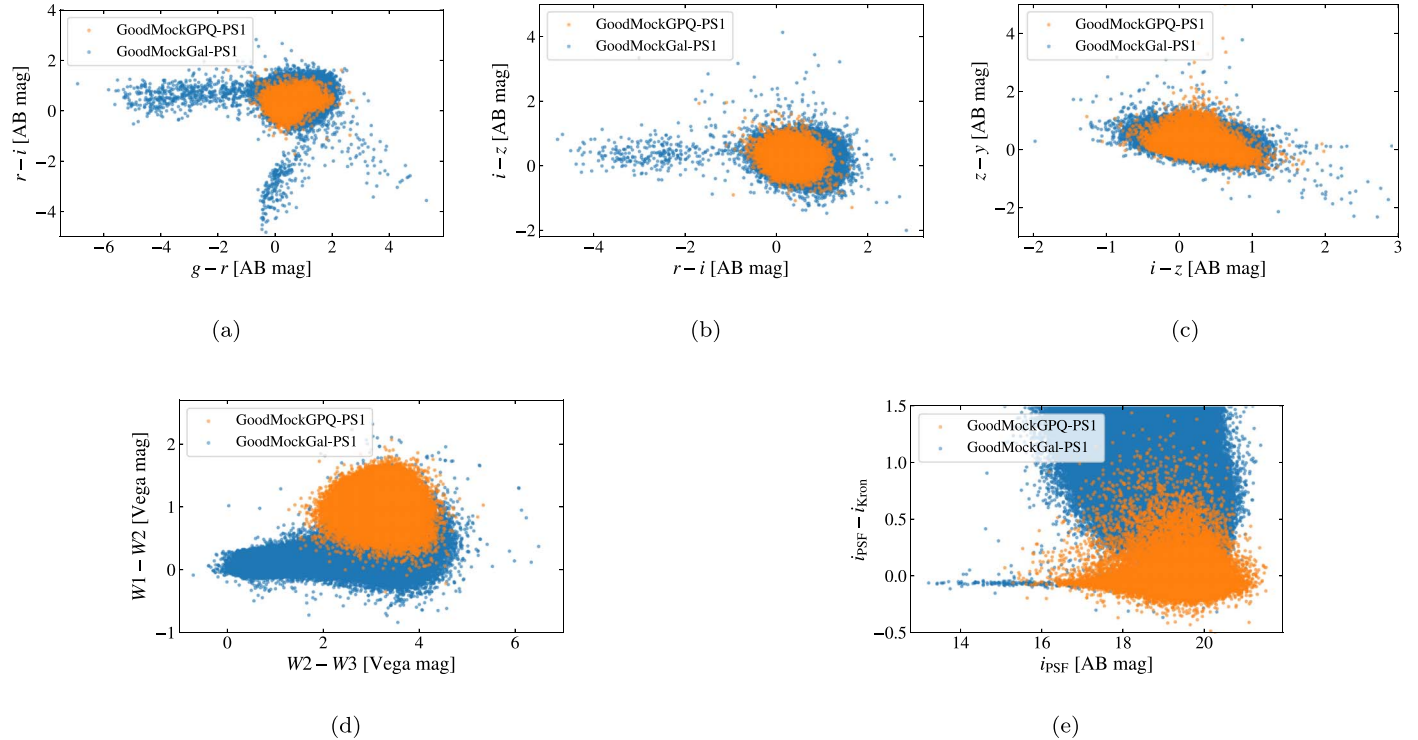


Figure 7. Color–color diagrams of GoodMockGPQ-PS1 and GoodMockGal-PS1 (a)–(d) and the $i_{\text{PSF}} - i_{\text{Kron}}$ vs. i_{PSF} plot for the two samples (e). Orange circles represent GoodMockGPQ-PS1 sources, while blue circles represent GoodMockGal-PS1 sources.

good photometry, as defined in Sections 2.1 and 2.2. The fraction $D_{\text{goodph}}/D_{\text{all}}$ roughly quantifies the effects of source crowdedness on the photometric quality. We expect that the median sky density of GPQs is no higher than that of GoodQSO ($\text{median}(D_{\text{new}}) \leq \text{median}(D_{\text{GoodQSO}})$); therefore, the

lower-limit “absolute” sky density of GPQs can be computed as

$$D_{\text{new}} \geq D'_{\text{new}} \times \frac{\text{median}(D_{\text{GoodQSO}})}{\text{median}(D'_{\text{new}})}, \quad (2)$$

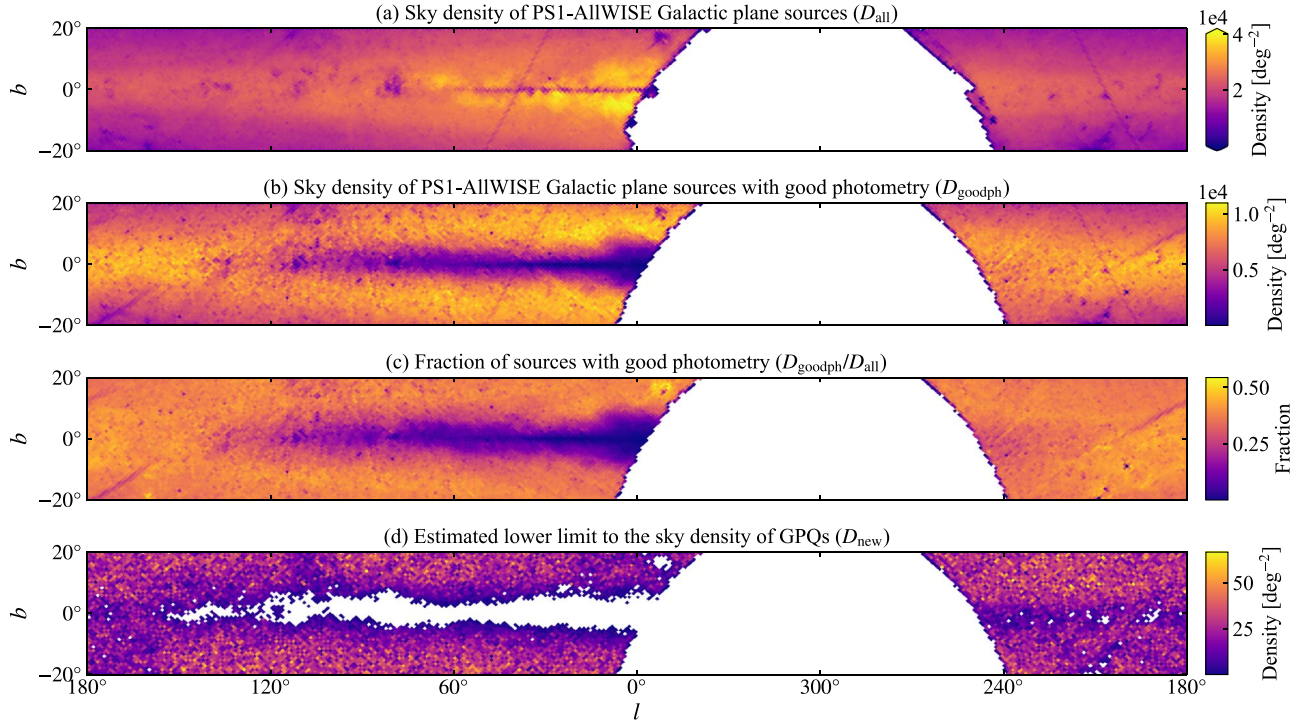


Figure 8. Sky density of all PS1-AllWISE Galactic plane sources (a) and the subset with good photometry (b), fraction of sources with good photometry in the PS1-AllWISE sample (c), and estimated lower limit to the sky density of GPQs (d).

where $\text{median}(D_{\text{GoodQSO}}) = 20.3 \text{ deg}^{-2}$, and $\text{median}(D'_{\text{new}}) = 2.9 \text{ deg}^{-2}$. Figure 8 shows the sky distribution of D_{all} , D_{goodph} , $D_{\text{goodph}}/D_{\text{all}}$, and D_{new} . The estimated D_{new} has a median of 20.3 deg^{-2} and a maximum of 66.7 deg^{-2} .

The predicted marginal probability of GPQs to the PS1-AllWISE sample with good photometry is $D_{\text{new}}/D_{\text{goodph}}$, which ranges from 2×10^{-4} to 0.17 with a median of 3×10^{-3} . The maximum value of 0.17 is not reliable because it is located at the edges of the HEALPix map ($\delta \sim -30^\circ$), where the source count in a pixel does not correspond to the true number of sources in the sky region.

5. GPQ Candidate Selections with XGBoost

We use XGBoost (Chen & Guestrin 2016), a scalable tree boosting system, to perform machine-learning classification for GPQ selection. It is an implementation of the original gradient-boosting framework (Friedman et al. 2000; Friedman 2001) known for high efficiency and outstanding performance in machine-learning competitions (Chen & Guestrin 2016). Compared to traditional gradient-boosting machines, XGBoost has made a few improvements at the algorithm level. For example, XGBoost includes regularization terms in the objective function to control the model complexity and therefore can reduce overfitting and improve the model generalization. It is optimized for sparse input data, i.e., data with missing values. Other than the greedy algorithm by Friedman (2001), XGBoost supports a weighted quantile sketch algorithm that can more effectively find the optimal split points. Moreover, system enhancements for parallelization, tree pruning, and cache optimization have been integrated into XGBoost. Recently, XGBoost has been applied to astronomy and showed its capabilities in handling astronomical problems, including identifying Galactic candidates among unassociated sources from the Third Fermi Large Area

Telescope catalog (Acero et al. 2015; e.g., Mirabal et al. 2016), distinguishing M giants from M dwarfs for spectral surveys (e.g., Yi et al. 2019), and selecting quasar candidates with photometric data (e.g., Jin et al. 2019).

In order to obtain the optimal models, we use optuna (Akiba et al. 2019), a hyperparameter optimization framework to tune the learning hyperparameters. As has been mentioned in Section 3.3, we transform the three-class classification problem into two binary classification problems (stars versus extragalactic objects and galaxies versus quasars). Under this setting, hyperparameters can be fine-tuned separately for the two classification steps. After classifying the Galactic plane sources with the two classifiers, we may use necessary additional criteria to ensure the purity of GPQ candidates. The classification scheme is shown in Figure 9.

A few evaluation metrics are used in the machine-learning process: accuracy, precision, recall, F_1 , Matthews correlation coefficient (MCC), and area under the precision-recall curve (AUCPR). With true positive denoted as TP, true negative as TN, false positive as FP, and false negative as FN, the first five metrics are defined as

$$\text{accuracy} = \frac{\text{TP} + \text{TN}}{\text{TP} + \text{TN} + \text{FP} + \text{FN}}, \quad (3)$$

$$\text{precision} = \frac{\text{TP}}{\text{TP} + \text{FP}}, \quad (4)$$

$$\text{recall} = \frac{\text{TP}}{\text{TP} + \text{FN}}, \quad (5)$$

$$F_1 = 2 \times \frac{\text{precision} \times \text{recall}}{\text{precision} + \text{recall}}, \quad (6)$$

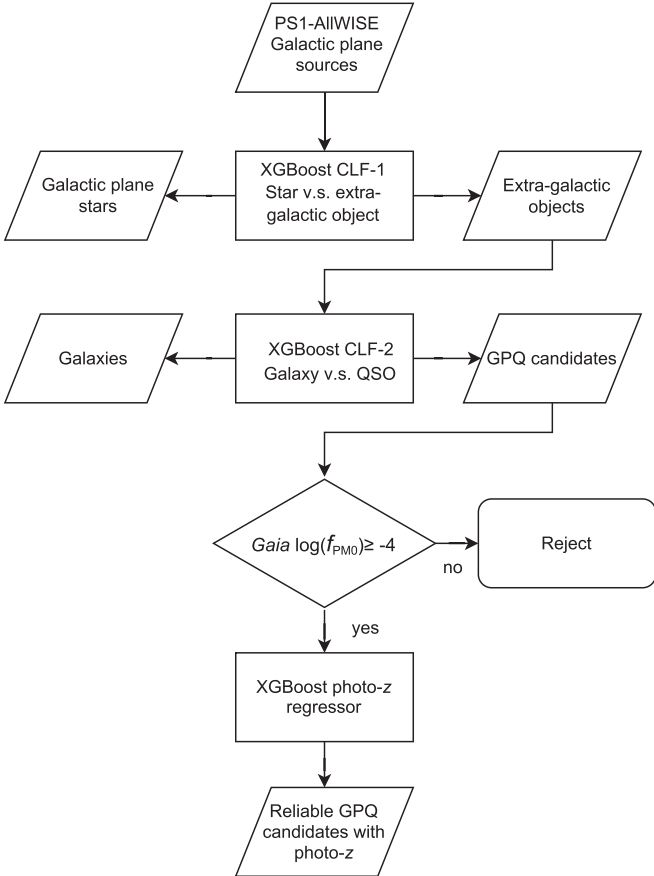


Figure 9. Flowchart of GPQ selection and photometric redshift calculation.

$$\text{MCC} = \frac{\text{TP} \times \text{TN} - \text{FP} \times \text{FN}}{\sqrt{(\text{TP} + \text{FP})(\text{TP} + \text{FN})(\text{TN} + \text{FP})(\text{TN} + \text{FN})}}. \quad (7)$$

The precision–recall (PR) curve can be constructed by plotting PR pairs (operating points) that are obtained using different thresholds on a probabilistic or other continuous-output classifier (Boyd et al. 2013). The AUCPR can then be calculated with numerical integration methods.

Among the six metrics, accuracy, precision, recall, and F_1 are commonly used. However, the accuracy and F_1 metrics fail to measure the classification performance correctly under class-imbalanced situations because they will be heavily biased toward the majority class. For example, given a sample with 95 from the negative class and five from the positive class, simply classifying all instances as negative produces accuracy = 0.95 and F_1 = 0.9744. These two scores of metrics are misleading because all of the positive instances are wrongly classified, while the accuracy and F_1 are high. The last two metrics, MCC and AUCPR, are considered better evaluation measures in class-imbalanced cases. The MCC takes the four confusion matrix categories (TP, TN, FP, and FN) into account, and it is high only if the classifier makes good predictions on both positive and negative classes, independently of their ratios in the overall data set (Chicco & Jurman 2020). It is also suggested by studies that the PR curve is more informative than the more famous receiver operator characteristic curve (first recommended by Provost et al. 1998), especially on imbalanced data sets (Davis & Goadrich 2006; Saito & Rehmsmeier 2015).

The AUCPR is useful as a measure of the overall performance of the model.

A total of 13 features are chosen for the two classification steps and the later photometric redshift regression, including 11 colors, $g - r$, $r - i$, $i - z$, $z - y$, $g - W_1$, $r - W_1$, $i - W_1$, $z - W_1$, $y - W_1$, $W_1 - W_2$, and $W_2 - W_3$, and two morphological features, $i - i_{\text{Kron}}$ and $z - z_{\text{Kron}}$. As has been discussed in Section 4.2, using a set of PS1 colors ($g - r$, $r - i$, $i - z$, and $z - y$) can help reduce the overlap between clusters of quasars and stellar loci on two-dimensional diagrams. Quasars have redder $W_1 - W_2$ and $W_2 - W_3$ colors than stars and galaxies, which makes these two colors good features for quasar selection. Jin et al. (2019) showed that three PS1-AllWISE colors (i.e., $i - W_1$, $y - W_1$, and $z - W_2$) can be used to efficiently distinguish quasars from stars and improve the performance of XGBoost classification. We construct similar colors as features by combining all PS1 bands and W_1 (i.e., $g - W_1$, $r - W_1$, $i - W_1$, $z - W_1$, and $y - W_1$) because W_1 is the most sensitive of the AllWISE bands. These five new colors provide rough optical SEDs for the objects and can characterize different objects with broader wavelength ranges than other optical colors (e.g., $g - r$) do. The differences between PSF and Kron magnitudes in the i_{P1} and z_{P1} bands ($i - i_{\text{Kron}}$ and $z - z_{\text{Kron}}$) are used as morphological features to separate point sources (stars and quasars) from extended sources (galaxies). We convert Vega magnitude to AB magnitude for AllWISE data when constructing all of the features. As we do not set constraints on W_3 magnitude or $W_3\text{snr}$ (S/N in W_3), some sources may have poor or missing W_3 (and $W_2 - W_3$) data. Nevertheless, the use of $W_2 - W_3$ will not be a problem because XGBoost can handle the missing values, and data with lower S/Ns are more informative than missing values.

5.1. Binary Classification for Stars and Extragalactic Objects

In the first classification step, the input data for training and validation consist of synthetic quasar sample T_{QSO} , synthetic galaxy sample T_{Gal} (see Section 4.1), and LAMOST Galactic plane star sample T_{Star} (Section 2.6). The input data have more than 3 million rows. For binarization, we assign the label EXT (extragalactic object) to all T_{QSO} and T_{Gal} instances and keep the label for T_{Star} as STAR. Here we regard extragalactic objects as the positive class and stars as the negative class.

We first apply fivefold cross-validations with optuna to find the optimal setting of the hyperparameters that minimizes the log loss among 500 trials. For a binary classification problem with a true label $y \in \{0, 1\}$ and a probability estimate $p = \text{Pr}(y = 1)$, the log loss per sample is the negative log-likelihood of the classifier given the true label:

$$\text{log_loss}(y, p) = -\log \text{Pr}(y|p) \quad (8)$$

$$= -(y \log(p) + (1 - y)\log(1 - p)). \quad (9)$$

Then we randomly split all of the input data into training and validation sets according to a 4:1 ratio and calculate the scores of the six metrics with the validation set. This 4:1 split ratio is consistent with that of the fivefold cross-validations. The large sample size of the input data also ensures that both the training and validation sets have enough samples.

Some fixed parameters in our programs are `objective = binary:logistic`, `booster = gbtree`, and `tree_method = hist`. For hyperparameters that are tuned, the

Table 2
Default and Optimal Hyperparameter Settings for CLF-1 (Star vs. Extragalactic Object Classification)

Hyperparameter	Default	Optimal
eta (learning_rate)	0.3	0.3
lambda (reg_lambda)	1	2.32
alpha (reg_alpha)	0	1.13
max_depth	6	9
gamma (min_split_loss)	0	0.60
grow_policy	depthwise	depthwise
min_child_weight	1	1
subsample	1	0.96
colsample_bytree	1	0.92
max_delta_step	0	3
Accuracy	0.9993	0.9995
Precision ⁺	0.9993	0.9995
Recall ⁺	0.9995	0.9996
F_1	0.9994	0.9996
MCC	0.9985	0.9990
AUCPR	0.9992	0.9995

default values, the optimal values found by the cross-validations, and the corresponding metric scores of these parameters are listed in Table 2. The number of boosting rounds (`num_boost_round`, aka `n_estimators` in the scikit-learn API of XGBoost) is fixed to 100 and not tuned together with `eta` (aka `learning_rate`) because the effects of increasing `num_boost_round` can cancel those of decreasing `eta`, and vice versa. In the training process, we need to lower the learning rate `eta` and increase the `num_boost_round` to reduce the generalization error. Classifier No. 1 (CLF-1) is trained using `eta = 0.02`, `num_boost_round = 1200` with other optimal parameters in Table 2.

We then classify the PS1-AllWISE pointlike sources with CLF-1. To exclude as many stars as possible, we adopt a high threshold on p_{EXT} (model-predicted probabilities of sources being extragalactic) to select extragalactic candidates. Sources with $p_{\text{EXT}} > 0.99$ are labeled as EXT, and the others are labeled as STAR and removed.

5.2. Binary Classification for Galaxies and Quasars

We use the T_{QSO} and T_{Gal} samples as input data for training and validation in the second classification step. Here we regard quasars as the positive class and galaxies as the negative class.

The same processes of parameter tuning and training as for CLF-1 are applied to build CLF-2. We keep some parameters unchanged: `objective=binary:logistic`, `booster=gbtree`, and `tree_method=hist`. For hyperparameters that are tuned, the default values, the optimal values found by the cross-validations, and the corresponding metric scores of these parameters are listed in Table 3. The CLF-2 is trained using `eta = 0.02`, `num_boost_round = 1500` with other optimal parameters in Table 3.

The optimal scores of the six metrics in Table 3 are all lower than those in Table 2, indicating that the quasar–galaxy classification “hardness” is higher than that of the star–extragalactic problem. Here we also use a high threshold of probability to select the sources of our target class. We classify the sources labeled as EXT with CLF-2. Sources with $p_{\text{QSO}} > 0.95$ are kept as GPQ candidates, where p_{QSO} is the

Table 3
Default and Optimal Hyperparameter Settings for CLF-2 (Quasar vs. Galaxy Classification)

Hyperparameter	Default	Optimal
eta (learning_rate)	0.3	0.2
lambda (reg_lambda)	1	2.32
alpha (reg_alpha)	0	1.10
max_depth	6	9
gamma (min_split_loss)	0	0.81
grow_policy	depthwise	depthwise
min_child_weight	1	2
subsample	1	0.95
colsample_bytree	1	0.86
max_delta_step	0	6
Accuracy	0.9969	0.9974
Precision ⁺	0.9894	0.9905
Recall ⁺	0.9894	0.9918
F_1	0.9894	0.9912
MCC	0.9875	0.9896
AUCPR	0.9938	0.9951

probability of a source being a quasar predicted by the XGBoost model.

5.3. Additional Cut Based on Gaia Proper Motion to Remove Stellar Contaminants

In the first classification process, we classify all PS1-AllWISE pointlike sources as stars and extragalactic objects. We ignore stars in the second classification step. Although the metrics of CLF-1 are high (Table 2), some stars can be misclassified as extragalactic objects and then classified as either quasars or galaxies. Faint stars are more likely to be misclassified than bright stars because the stars in the training sample (T_{Star}) are biased toward the bright end. When using optical and near-IR colors for candidate selection, white dwarfs are major contaminants for low-redshift quasars, and M/L/T dwarfs are typical contaminants for high-redshift quasars (e.g., Kirkpatrick et al. 1997; Vennes et al. 2002; Chiu et al. 2006). In the mid-IR regime, potential stellar contaminants for quasars are YSOs, asymptotic giant branch (AGB) stars, and planetary nebulae (PNe; Kozłowski & Kochanek 2009; Koenig & Leisawitz 2014; Assef et al. 2018).

The YSOs are stars at the early stages of evolution and are often divided into four subclasses (Lada 1987; Andre et al. 1993): class I, class II, flat-spectrum, and class III. Among them, class II and flat-spectrum YSOs are the most likely contaminants, since they have optical and mid-IR SEDs similar to those of quasars. Since we require both optical and mid-IR detections for classification, optically faint class I YSOs are eliminated in the first place. As has been studied by Koenig & Leisawitz (2014), class III YSOs are clustered around $W_2 - W_3 = 0$ and $W_1 - W_2 = 0$, while class I and II and flat-spectrum YSOs occupy the region with approximately $W_1 - W_2 > 0.25$ and $1.0 < W_2 - W_3 < 4.5$ (see their Figure 5). The latter YSO region is overlapped with the quasar region shown in Figure 6; therefore, the contamination should be taken care of.

The AGB stars are evolved stars with low temperatures and high luminosities. They are surrounded by circumstellar envelopes, and IR excess exists in their broad SEDs. According to Figure 5 from Koenig & Leisawitz (2014), only a minority

of AGB stars actually overlap with class I and II and flat-spectrum YSOs (and thus quasars) in the W1 – W2 versus W2 – W3 diagram. Therefore, we expect that the contamination from AGB stars is less than that from YSOs.

The PNe have a series of narrow emission lines, as well as IR excess. Known PNe can be later removed from the GPQ candidate sample by cross-matching with the Simbad database (Wenger et al. 2000).

In order to remove stellar contaminants such as white dwarfs, M/L/T dwarfs, YSOs, and AGB stars from GPQ candidates, we apply an additional cut based on Gaia proper motion, because the proper-motion distribution of quasars is different from that of Milky Way stars. Although quasars should have negligible transverse motions, their nonzero proper motions are measured by Gaia due to various effects, such as the photocenter variability of quasars (see Bachchan et al. 2016, and references therein). In addition, proper motions with large uncertainties are not reliable. Therefore, we need a probabilistic cut instead of a cut on the total proper motion. We define the probability density of zero proper motion ($f_{\text{PM}0}$) of a source based on the bivariate normal distribution of proper-motion measurements of the source as

$$f_{\text{PM}0} = \frac{1}{2\pi\sigma_x\sigma_y\sqrt{1-\rho^2}} \exp \left\{ -\frac{1}{2(1-\rho^2)} \times \left[\left(\frac{x}{\sigma_x} \right)^2 - \frac{2\rho xy}{\sigma_x\sigma_y} + \left(\frac{y}{\sigma_y} \right)^2 \right] \right\}, \quad (10)$$

where $x = \text{pmra}$, $y = \text{pmdec}$, and $\rho = \text{pmra_pmdec_corr}$ (correlation coefficient between pmra and pmdec) are obtained from the Gaia DR2 catalog, while σ_x and σ_y are the true external proper-motion uncertainties calculated with the method suggested by Lindegren et al. (2018a, 2018b). The external proper-motion uncertainty can be expressed as $\sigma_{\text{ext}} = (k^2\sigma_i^2 + \sigma_s^2)^{\frac{1}{2}}$, where σ_{ext} can be σ_x or σ_y , $k = 1.08$ is a multiplicative factor, σ_i is the catalog uncertainty (pmra_error or pmdec_error), and σ_s is the systematic error. For bright sources ($G < 13$), $\sigma_s = 0.032 \text{ mas yr}^{-1}$; for faint sources ($G > 13$), $\sigma_s = 0.066 \text{ mas yr}^{-1}$. Under the same uncertainty level, sources with smaller proper motions will have higher $f_{\text{PM}0}$ by definition.

We take the logarithm of $f_{\text{PM}0}$ for better comparison between samples. Figure 10 shows the distributions of the $\log(f_{\text{PM}0})$ of stars, galaxies, and quasars used in this study. For stellar samples, in addition to T_{Star} (LAMOST Galactic plane star sample), a subsample of the SDSS Stripe 82 Standard Star Catalog (hereafter S82 star; Ivezić et al. 2007) that meets the same constraints in Sections 2.1 and 2.2 is also included for comparison. We choose a $\log(f_{\text{PM}0}) \geq -4$ cut that excludes 94.1% of both LAMOST Galactic plane stars and S82 stars, while it retains 99.8% of the quasars. Nevertheless, faint stars can be major contaminants even with such a strict cut on $\log(f_{\text{PM}0})$.

We calculate the $\log(f_{\text{PM}0})$ for GPQ candidates after cross-matching them with Gaia DR2. For candidates without Gaia DR2 proper-motion records, we assign a default value of 99 for $\log(f_{\text{PM}0})$. Sources with $\log(f_{\text{PM}0}) \geq -4$ are kept as reliable GPQ candidates.

6. Photometric Redshift Estimation for GPQ Candidates

Measuring redshifts is an important step for quasar surveys. For quasar candidates, photometric redshift (photo- z) estimation is key to follow-up studies. Many different approaches have been proposed for calculating the photo- z s of quasars, including quasar template fitting (e.g., Budavári et al. 2001; Babbedge et al. 2004; Salvato et al. 2009), the empirical color-redshift relation (e.g., Richards et al. 2001; Weinstein et al. 2004; Wu et al. 2004, 2012; Wu & Jia 2010), machine learning (e.g., Yèche et al. 2010; Laurino et al. 2011; Brescia et al. 2013; Zhang et al. 2013; Pasquet-Itam & Pasquet 2018), the XDQSOz method (Bovy et al. 2012), and the Skew-QSO method (Yang et al. 2017). As the photo- z estimation problem can be well described by the regression problem in machine learning, we also use XGBoost to train the regression model and predict photo- z s for our reliable GPQ candidates.

To build the training and validation sets, we randomly split the dereddened GoodQSO sample with a ratio of 4:1. Our application set (reliable GPQ candidates) is also dereddened. The same 13 features as those in Section 5 are used for photo- z regression: $g - r$, $r - i$, $i - z$, $z - y$, $g - W1$, $r - W1$, $i - W1$, $z - W1$, $y - W1$, $W1 - W2$, $W2 - W3$, $i - i_{\text{Kron}}$, and $z - z_{\text{Kron}}$. The morphological features $i - i_{\text{Kron}}$ and $z - z_{\text{Kron}}$ are included because they may help distinguish quasars at different cosmological distances. To obtain the optimal model, we also tune the parameters with fivefold cross-validations using optuna.

The performance of the XGBoost photo- z regression model on the validation set can be examined in the $z_{\text{phot}} - z_{\text{spec}}$ (photometric redshift versus spectral redshift) plot (Figure 11) or with two quantities: the rms error (RMSE) and photo- z accuracy. For a validation set with a sample size n , the RMSE is $\text{RMSE} = \sqrt{\sum_{i=1}^n (z_{\text{phot}} - z_{\text{spec}})^2 / n}$. In our validation set with a sample size of 57,855, the RMSE is 0.35. The photo- z accuracy $R_{0.1}$ is defined as the fraction of quasars with $|\Delta z| \leq 0.1$, where $|\Delta z| = |z_{\text{spec}} - z_{\text{phot}}| / (1 + z_{\text{spec}})$. Our XGBoost regression model yields a photo- z accuracy of 74% on the validation set, which is comparable to that of Yang et al. (2017) on PS1 and WISE data (79%). Yang et al. (2017) adopted a multivariate Skew-t model and prior probabilities from the quasar luminosity function to achieve the high photo- z accuracy. Figure 12 shows the photo- z accuracy $R_{0.1}$ as a function of spectral redshift (left panel) and dereddened i_{P1} -band magnitude (right panel). Here $R_{0.1}$ has maximum values at $z \approx 2.3$ and 4 and reaches a minimum at $z \approx 3$. Most $z \approx 3$ quasars have underestimated photometric redshifts (see Figure 11) due to a degeneracy of broadband photometry in response to quasar SEDs at different redshifts. The strong Ly α emission line enters the g_{P1} band at $z \approx 2.4$ and moves into the r_{P1} band at $z \approx 3.5$, which leads to a large excess in g_{P1} magnitudes and hence similar PS1 colors of quasars within $2.4 \lesssim z \lesssim 3.5$. This kind of degeneracy can be alleviated if SDSS u -band data are available to characterize the Lyman-limit systems (see Section 4 of Yang et al. 2017). The photo- z accuracy is improved at $z \gtrsim 3.5$ because the Lyman limit enters the g_{P1} band. The $R_{0.1}$ also drops at low redshift ($z < 1$) and both the bright and faint ends because the training sample is biased toward intermediate redshifts and magnitudes.

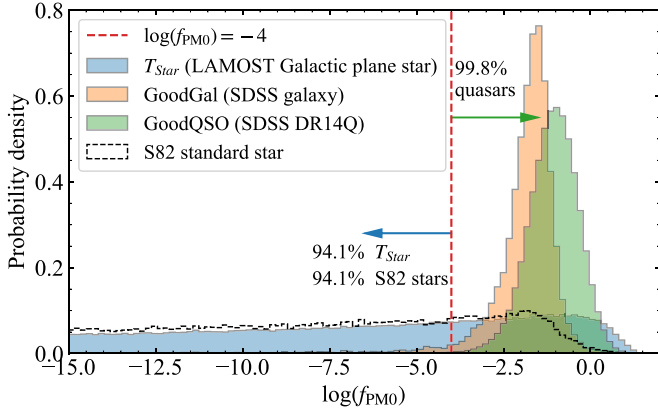


Figure 10. Histograms of the $\log(f_{\text{PMO}})$ of T_{Star} (LAMOST Galactic plane star), GoodGal (from SDSS galaxy), GoodQSO (from SDSS DR14Q), and sources from the S82 star. Because f_{PMO} is the probability density, which can be greater than 1 (the integral of the probability density function over the entire space is equal to 1), $\log(f_{\text{PMO}})$ can have positive values.

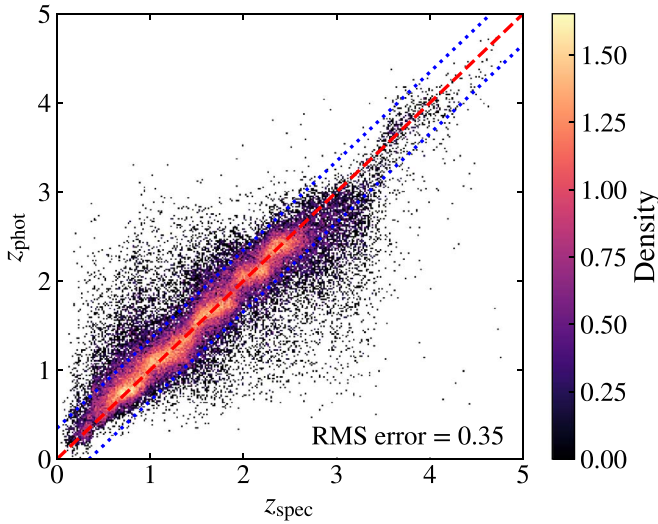


Figure 11. Photometric redshift obtained with the XGBoost regression model against the spectral redshift of the dereddened validation set with 57,855 quasars. The red dashed line denotes $z_{\text{phot}} = z_{\text{spec}}$, and the blue dotted lines mark the margin within one RMSE from the red dashed line.

7. The GPQ Candidate Catalog

7.1. Validation of the GPQ Candidates with Simbad, Milliquas, and SDSS DR16Q

With our transfer-learning framework and the aforementioned additional selection criteria, we obtain a reliable GPQ candidate sample with 161,532 sources from PS1 and AllWISE. We cross-match the GPQ candidates with the Simbad database (Wenger et al. 2000) and find 2786 matches. The object types and summary are shown in Table 4.

We categorize all matched sources into four groups: AGNs/QSOs, stars (including PNe and PN candidates), galaxies, and other types of objects. Among all of the matches, 53.98% (1504) are recorded as AGNs/QSOs (including candidates), 8.97% (250) are recorded as stars (including candidates), 4.02% (112) are recorded as galaxies, and 33.02% (920) are other types of objects labeled according to their detection properties (e.g., wavelength). Those other types of objects have higher probabilities of being AGNs/QSOs than stars, as most (728+27) of them are radio sources and 64 are X-ray sources

(see Table 4). For the 4.02% of sources labeled as galaxies, a number of them may also host AGNs/QSOs, as we have applied careful selection criteria to remove possible galaxy contaminants. Among the 250 sources labeled as stars, 40 are candidates, and the other 210 are known stars. Of the known stars, 101 were once selected as QSO candidates using SDSS photometry and then identified as stars by the 2dF-SDSS LRG and QSO Survey (Croom et al. 2009). From these analyses, we can conclude that the purity of our GPQ candidates on the small subset of 2786 Simbad matches can be as high as $\sim 90\%$. The true purity may vary at different locations in the Galactic plane.

As another test of stellar contamination, we cross-match our GPQ candidates with the LAMOST Galactic plane star sample. This match identifies 29 LAMOST stars, none of which are recorded in Simbad. Therefore, the total number of known stars in the GPQ candidates is 239.

We also examine the fraction of known GPQs that can be recovered with our candidate table. The known GPQ sample is MLQSUB with 1853 sources, which is retrieved from the Milliquas catalog and described in Section 2.7. The MLQSUB is selected with the same constraints as those on our application PS1-AllWISE data to get a consistent analysis result. Cross-matching MLQSUB with our GPQ candidates results in 1763 matches, meaning that 95.14% of GPQs from Milliquas can be selected with our methods under the same quality constraints on the photometric data. The recent sixteenth data release of the SDSS Quasar Catalog (DR16Q; Lyke et al. 2020) has a total of 750,414 sources, of which 3737 sources are located at $|b| < 20^\circ$. Only 1320 of these SDSS GPQs meet the photometric quality constraints in Sections 2.1 and 2.2. Cross-matching our GPQ candidates with SDSS DR16Q gives 1292 matches, which corresponds to a recall rate of 97.88% under the same photometric quality constraints or 34.57% for the whole identified sample. The overall completeness of the sample of candidates is mainly limited by the photometric quality constraints.

7.2. Description of the GPQ Candidate Catalog

We remove 239 known stars (see Section 7.1) from our GPQ candidate sample. We then matched the remaining GPQ candidates by coordinates with TOPCAT internally and found 347 close pairs within $0.^{\circ}2$. These pairs are very likely duplicated sources, because the PS1 survey cannot resolve two sources within an angular distance of $0.^{\circ}2$. The median image quality for the PS1 3π survey is $\text{FWHM} = (1.^{\circ}31, 1.^{\circ}19, 1.^{\circ}11, 1.^{\circ}07, 1.^{\circ}02)$ for $(\text{grizy}_{\text{P1}})$ (Magnier et al. 2020). Therefore, we only keep one source for each close pair and obtain the final GPQ candidate sample with 160,946 sources. The GPQ candidate catalog is compiled based on this sample with photometric data from PS1 DR1 and AllWISE and astrometric data from Gaia DR2. The descriptions for the catalog are displayed in Table 5.

The sky density of sources from the GPQ candidate catalog is shown in Figure 13. In general, the sky distribution of the GPQ candidates is consistent with the prediction in Section 4.3. The highest sky density of the candidates is 72.7 deg^{-2} , which is slightly higher than the estimation (66.7 deg^{-2}). The median density is 16.7 deg^{-2} , which is comparable but lower than the estimated value (or the median density of GoodQSO). As can be seen from Figure 13, the sky densities of GPQ candidates at $|b| \lesssim 10^\circ$ are lower than those of the estimation in Figure 8(d),

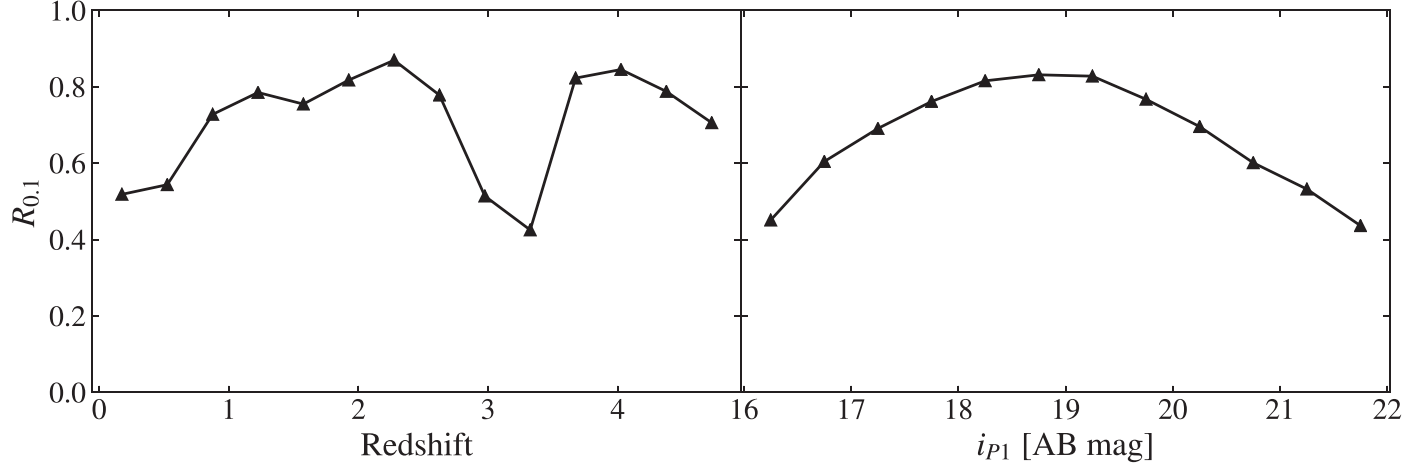


Figure 12. Photo- z accuracy $R_{0.1}$ (the fraction of quasars with $|\Delta z| \leq 0.1$, where $|\Delta z| = |z_{\text{spec}} - z_{\text{phot}}|/(1 + z_{\text{spec}})$) as a function of redshift (left panel) and magnitude (dereddened; right panel).

Table 4
Matching Results of GPQ Candidates and the Simbad Database

AGN/QSO	Number	Star	Number	Galaxy	Number	Other Types	Number
QSO	1121	Star	175	Galaxy	106	Radio source	728
AGN candidate	150	YSO candidate	22	Radio galaxy	3	IR source	77
BL Lac object	143	YSO	13	Brightest galaxy in a cluster	2	X-ray source	64
Seyfert 1 galaxy	38	Cataclysmic binary candidate	7	Cluster of galaxies	1	Centimetric radio source	27
AGN	31	PN	5			Blue object	22
Other subclasses	21	Other subclasses	28			Far-IR source ($\lambda \geq 30 \mu\text{m}$)	2
Total	1504	Total	250	Total	112	Total	920
Fraction	53.98%	Fraction	8.97%	Fraction	4.02%	Fraction	33.02%

which indicates that the modeling process overestimates the sky density of GPQs at lower Galactic latitudes. The region with $\delta \lesssim -30^\circ$ ($240^\circ \lesssim l \lesssim 360^\circ$) is blank because it is not covered by the PS1 3π survey.

The distributions of the dereddened i_{P1} magnitudes and photometric redshifts of our GPQ candidates are displayed in Figure 14(a). The lowest and highest photometric redshifts are $z_{\text{phot}} = 0.016$ and 4.777 , respectively. Taking into account the uncertainties in the photo- z estimations, the actual highest redshift of the GPQs can be up to 5 . Five peaks appear in the histogram of photometric redshift (Figure 14(a)) at $z_{\text{phot}} \approx (0.8, 1.2, 1.7, 2.1, 2.4)$, which are caused by the selection effects and sample bias of the training set. Quasars with these redshifts have higher chances of being selected with PS1 photometry: (i) when $z \approx 0.8$, the Mg II emission line enters the g_{P1} band; (ii) when $z \approx 1.2$, Mg II enters the r_{P1} band; (iii) when $z \approx 1.7$, C III] enters the g_{P1} band and Mg II enters the i_{P1} band; (iv) when $z \approx 2.1$, both the Si IV and C IV lines enter the g_{P1} band and C III] enters the r_{P1} band; and (v) when $z \approx 2.4$, Ly α and Si IV enter the g_{P1} band.

The distributions of the dereddened i_{P1} magnitudes and spectroscopic redshifts of the GoodQSO sample from SDSS DR14Q are also shown in Figure 14(b) for comparison. The GoodQSO sample and the sample of GPQ candidates have similar redshift distributions, with some subtle differences. The magnitude distributions are also similar to each other, except that GoodQSO has a larger fraction of bright sources ($i_{P1} < 19$) than the GPQ candidates. Such differences in both redshift and magnitude distributions of these two samples are mainly due to their different target selection strategies. Our GPQ candidates

are selected from a single parent sample, while SDSS DR14Q includes many quasar samples in various redshift and magnitude ranges (see Section 2.2 of Pâris et al. 2018).

The color–color properties of sources from the GPQ candidate catalog are shown in Figure 15. In general, GPQ candidates have color–color distributions that are well matched to those of *GoodMockQSO-PS1* (see Figures 5 and 6). The unimodal structures seen from both AllWISE and PS1 colors imply a low level of contamination from stars and galaxies. However, contamination from stars can be recognized from the $i - z$ versus $r - i$ diagram, where some sources are concentrated along the stellar locus (see the slightly contaminated region “SC” in Figure 15(c)). We apply no cut on the SC region because it only contains 7892 sources (4.90% of the whole catalog), and any cut is likely to also remove reddened quasars (see Figure 5).

8. Summary and Conclusions

We present a transfer-learning framework for quasar selection and its application to finding GPQs. We construct mock samples of quasars and galaxies behind the Galactic plane by assigning new locations and extinction values to the extinction-corrected high- b SDSS extragalactic sources. We use PS1 limiting magnitudes to select good mock sources and compare them with high- b sources in color–color spaces. We show that the covariate change of source colors is significant from high- b regions to the Galactic plane. We synthesize training and validation data for machine learning with (i) good mock samples, (ii) SDSS extragalactic sources that do not have

Table 5
Contents of the GPQ Candidate Catalog

Column	Units	Label	Explanations
1	...	Designation	Catalog designation hhmmss.ss+ddmmss.s (J2000) based on PS1 coordinates
2	deg	ra	PS1 R.A. in decimal degrees (J2000) (weighted mean) at mean epoch
3	deg	dec	PS1 decl. in decimal degrees (J2000) (weighted mean) at mean epoch
4	deg	l	Galactic longitude in decimal degrees
5	deg	b	Galactic latitude in decimal degrees
6	...	photoz	Photometric redshift predicted with XGBoost regressor
7	...	p_star	Probability of the object being a star, predicted by the first XGBoost classifier, aka p_{star} ($p_{\text{star}} + p_{\text{ext}} = 1$)
8	...	p_ext	Probability of the object being an extragalactic object, predicted by the first XGBoost classifier, aka p_{ext} ($p_{\text{star}} + p_{\text{ext}} = 1$)
9	...	p2_gal	Probability of the object being a galaxy, predicted by the second XGBoost classifier, aka p_{gal} ($p_{\text{gal}} + p_{\text{qso}} = 1$)
10	...	p2_qso	Probability of the object being a quasar, predicted by the second XGBoost classifier, aka p_{qso} ($p_{\text{gal}} + p_{\text{qso}} = 1$)
11	...	fpm0	Probability density of zero proper motion (f_{PM0}) of the source
12	...	log_fpm0	Logarithm of fpm0 ($\log(f_{\text{PM0}})$)
13	mag	ebv	Line-of-sight $E(B - V)$ given by the Planck14 dust map
14	...	PS_objID	PS1 unique object identifier
15	mag	gmag	Mean PSF AB magnitude from PS1 g-filter detections
16	mag	e_gmag	Error in gmag
17	mag	gKmag	Mean Kron AB magnitude from PS1 g-filter detections
18	mag	e_gKmag	Error in gKmag
19	mag	rmag	Mean PSF AB magnitude from PS1 r-filter detections
20	mag	e_rmag	Error in rmag
21	mag	rKmag	Mean Kron AB magnitude from PS1 r-filter detections
22	mag	e_rKmag	Error in rKmag
23	mag	imag	Mean PSF AB magnitude from PS1 i-filter detections
24	mag	e_imag	Error in imag
25	mag	iKmag	Mean Kron AB magnitude from PS1 i-filter detections
26	mag	e_iKmag	Error in iKmag
27	mag	zmag	Mean PSF AB magnitude from PS1 z-filter detections
28	mag	e_zmag	Error in zmag
29	mag	zKmag	Mean Kron AB magnitude from PS1 z-filter detections
30	mag	e_zKmag	Error in zKmag
31	mag	ymag	Mean PSF AB magnitude from PS1 y-filter detections
32	mag	e_ymag	Error in ymag
33	mag	yKmag	Mean Kron AB magnitude from PS1 y-filter detections
34	mag	e_yKmag	Error in yKmag
35	...	AllWISE_ID	AllWISE unique source ID
36	mag	W1mag	W1 (Vega) magnitude ($3.35 \mu\text{m}$)
37	mag	e_W1mag	Mean error on W1 magnitude
38	mag	W2mag	W2 (Vega) magnitude ($4.6 \mu\text{m}$)
39	mag	e_W2mag	Mean error on W2 magnitude
40	mag	W3mag	W3 (Vega) magnitude ($11.6 \mu\text{m}$)
41	mag	e_W3mag	Mean error on W3 magnitude
42	mag	W4mag	W4 (Vega) magnitude ($22.1 \mu\text{m}$)
43	mag	e_W4mag	Mean error on W4 magnitude
44	mag	Jmag	2MASS J (Vega) magnitude ($1.25 \mu\text{m}$)
45	mag	e_Jmag	Mean error on J magnitude
46	mag	Hmag	2MASS H (Vega) magnitude ($1.65 \mu\text{m}$)
47	mag	e_Hmag	Mean error on H magnitude
48	mag	Kmag	2MASS Ks (Vega) magnitude ($2.17 \mu\text{m}$)
49	mag	e_Kmag	Mean error on Ks magnitude
50	...	Gaia_source_id	Gaia DR2 unique source identifier
51	mas	parallax	Gaia DR2 parallax
52	mas	parallax_error	Standard error of parallax
53	mas yr^{-1}	pmra	Gaia DR2 proper motion in R.A. direction
54	mas yr^{-1}	pmra_error	Standard error of pmra
55	mas yr^{-1}	pmdec	Gaia DR2 proper motion in decl. direction
56	mas yr^{-1}	pmdec_error	Standard error of pmdec
57	...	pmdec_pmdec_corr	Correlation between pmra and pmdec
58	mas yr^{-1}	pmra_error_ext	True external uncertainty of pmra
59	mas yr^{-1}	pmdec_error_ext	True external uncertainty of pmdec
60	...	sb_main_id	Main identifier for an object in Simbad database
61	...	sb_main_type	Main object type for an object in Simbad database
62	...	sb_redshift	Redshift of an object recorded in Simbad database

(This table is available in its entirety in FITS format.)

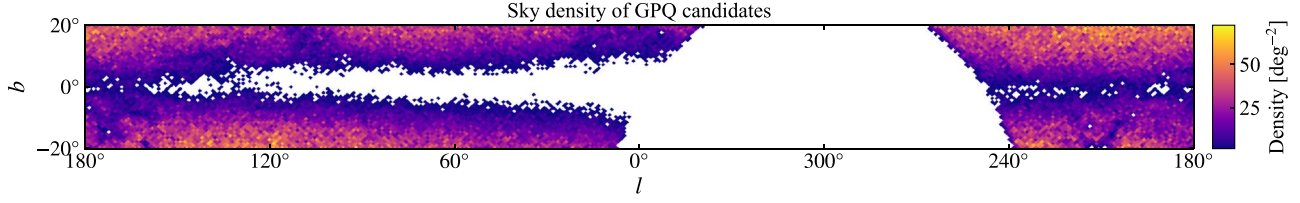
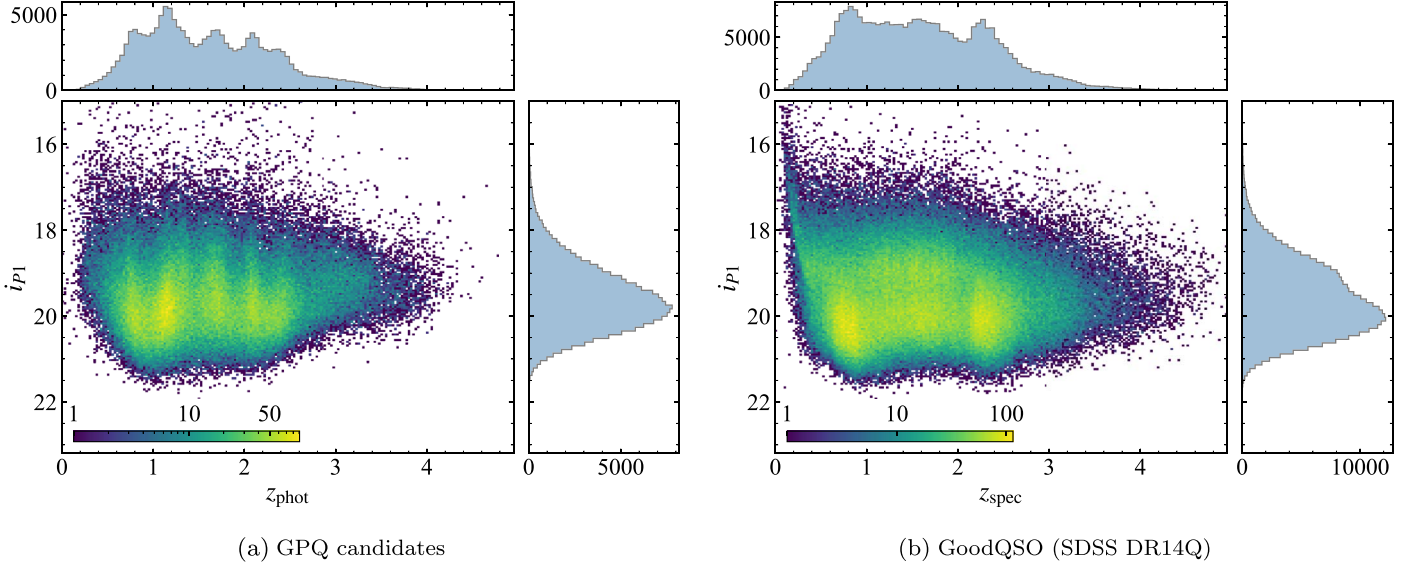


Figure 13. Sky density plot of GPQ candidates in Galactic coordinates.

Figure 14. (a) Dereddened i_{P1} magnitude and photometric redshift distribution of GPQ candidates. (b) Dereddened i_{P1} magnitude and redshift distribution of the GoodQSO sample. The i_{P1} magnitude is dereddened according to the Planck14 dust map.

counterparts in the good mock samples, and (iii) a real LAMOST Galactic plane star sample.

We apply the XGBoost algorithm for machine learning in this study. To help reduce the effects of class imbalance and class-balance change, we turn the three-class classification task (star, galaxy, and quasar) into two binary classification problems. A total of 13 features are used for the two classification steps: $g - r$, $r - i$, $i - z$, $z - y$, $g - W1$, $r - W1$, $i - W1$, $z - W1$, $y - W1$, $W1 - W2$, $W2 - W3$, $i - i_{\text{Kron}}$, and $z - z_{\text{Kron}}$. In order to remove star and galaxy contaminants, we use high thresholds of model-predicted probabilities ($p_{\text{EXT}} > 0.99$ and $p_{\text{QSO}} > 0.95$) to select extragalactic and quasar candidates. We perform an additional cut on the probability density of zero proper motion ($\log(f_{\text{PM0}}) \geq -4$) based on Gaia DR2 data to further reduce stellar contamination. Using the extinction-corrected SDSS DR14Q sources, we build the photometric redshift estimator with RMSE = 0.35 on the validation set.

Our GPQ candidate sample is validated with the Simbad database and Milliquas catalog. The purity of quasars is $\sim 90\%$ on the Simbad matches. Under our constraints for good PS1 and AllWISE photometry, 95.14% of the GPQs in the Milliquas catalog and 97.88% of the GPQs from SDSS DR14Q can be recalled with our GPQ candidate sample. The photometric quality constraints ensure the reliability of the candidates but at the cost of lower overall completeness of the candidate sample. The sky density of GPQ candidates is consistent with the estimation based on the mock GPQ catalog. The median marginal probability of GPQs to the PS1-AllWISE

sample with good photometry is $\sim 10^{-3}$, and the lowest marginal probability is $\sim 10^{-4}$. We compile the GPQ candidate catalog after removing known stars in Simbad and LAMOST and some duplicated sources. The GPQ candidate catalog consists of 60,946 sources. In addition to our machine-learning predictions, we include PS1 and AllWISE photometry, as well as Gaia DR2 astrometry in the table. The GPQ candidate sample has broad redshift coverage ($0 < z \lesssim 5$), indicating that our selection methods can be used on wide redshift ranges.

The colors of the GPQ candidates agree well with those of the mock GPQ catalog, which also indicates a high purity of the candidates even though the marginal probability is low. Contamination from stars and galaxies still exists in the GPQ candidate sample but at a low level. Because most stars in the training sample (T_{Star}) are bright, identifying and removing faint stars can be challenging for the XGBoost classification model (CLF-1). Using colors instead of magnitudes as features helps to lessen the effects of such training sample bias. The strict $\log(f_{\text{PM0}}) \geq -4$ cut can additionally remove most stellar contaminants. Galaxies overlap heavily with quasars on PS1 color-color diagrams and show a similar $\log(f_{\text{PM0}})$ distribution with quasars. The use of AllWISE colors ($W1 - W2$ and $W2 - W3$) and morphological separators ($i - i_{\text{Kron}}$ and $z - z_{\text{Kron}}$) largely aids the galaxy-quasar classification. For future GPQ candidate selections, we expect to improve the machine-learning performance by compiling a Galactic plane star training sample with more stars in the faint end.

We have been carrying out a series of spectroscopic identifications of GPQ candidates since 2018 using optical

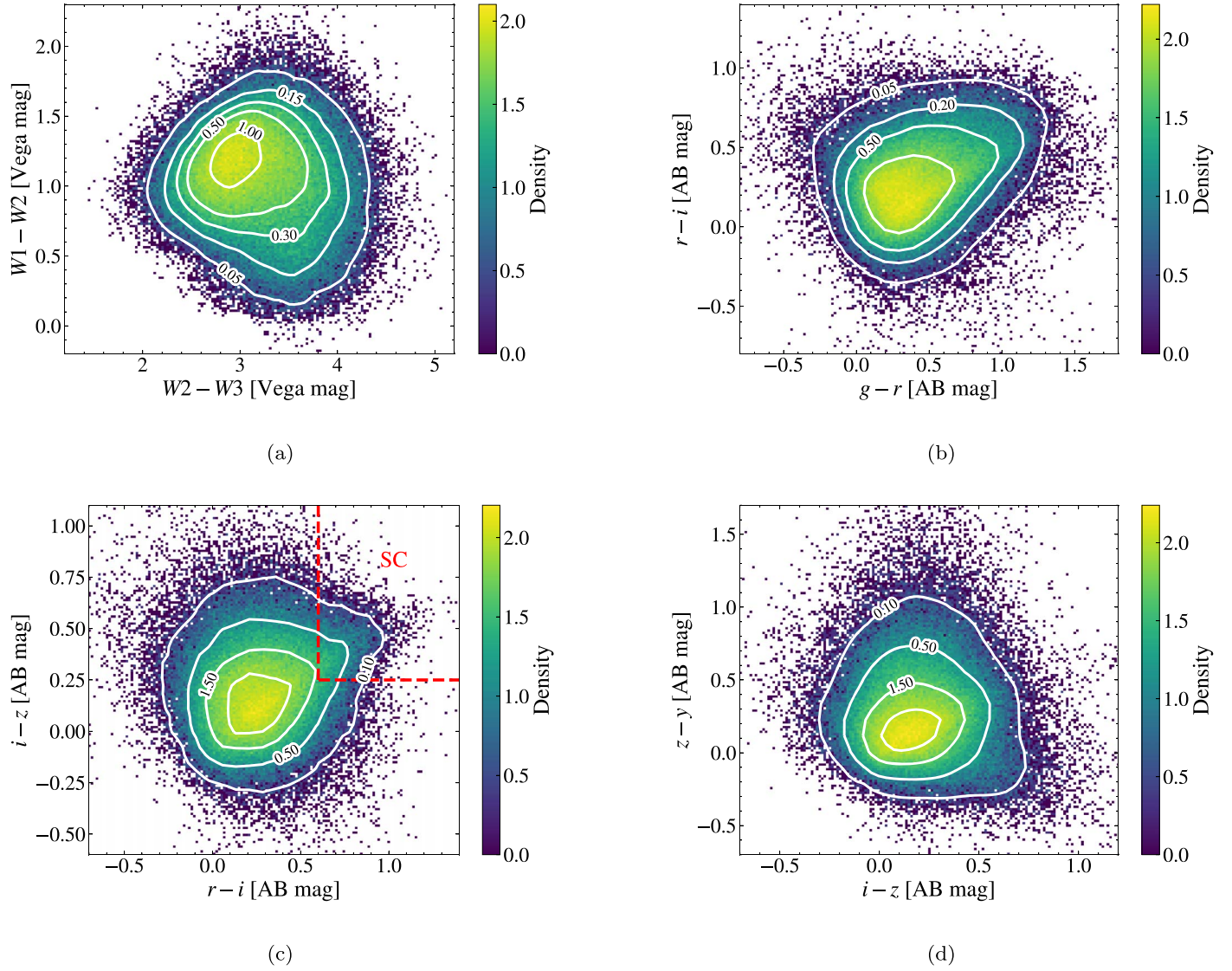


Figure 15. AllWISE (a) and PS1 (b)–(d) color–color diagrams of sources from the GPQ candidate catalog. Contour lines based on two-dimensional kernel density estimation are displayed on the density plots. The red dashed lines and SC in panel (c) mark the region that is slightly contaminated by stars ($r - i > 0.6$ and $i - z > 0.25$).

telescopes, including the 2 m telescopes based at Lijiang and Xinglong in China and Siding Spring in Australia and the 200 inch Hale Telescope in the US. The success rate of identifying new GPQs is $\sim 90\%$ in our spectroscopic campaign, which is consistent with the estimated reliability of the GPQ candidate catalog. We have also been exploring the LAMOST spectral data to find new GPQs. All of these efforts have yielded promising results that will be presented in the next paper of this series.

We are thankful for the support of the National Key R&D Program of China (2016YFA0400703) and the National Science Foundation of China (11533001, 11721303, and 11927804). We thank the referee very much for constructive and helpful suggestions to improve this paper. We thank Prof. Yanxia Zhang (NAOC) for helping us cross-match the PS1 and AllWISE catalogs. We thank Dr. Jinyi Yang and Dr. Feige Wang from Steward Observatory for useful suggestions. Y.F. thanks Dr. Hassen Yesuf (KIAA-PKU), Dr. Bojin Zhuang (Ping An Technology), Hongdong Zheng (PKU), and Dinghuai

Zhang (Mila/PKU) for helpful discussions on machine learning. Y.F. thanks Prof. Gregory J. Herczeg, Bitao Wang, Mingyang Zhuang, Yun Zheng, Yuanhang Ning, and Niankun Yu from PKU for helping edit the draft.

This research makes use of the cross-match service provided by CDS, Strasbourg. This publication makes use of data from the Pan-STARRS1 Surveys. The Pan-STARRS1 Surveys (PS1) and the PS1 public science archive have been made possible through contributions by the Institute for Astronomy, the University of Hawaii, the Pan-STARRS Project Office, the Max Planck Society and its participating institutes, the Max Planck Institute for Astronomy, Heidelberg and the Max Planck Institute for Extraterrestrial Physics, Garching, The Johns Hopkins University, Durham University, the University of Edinburgh, the Queen’s University Belfast, the Harvard-Smithsonian Center for Astrophysics, the Las Cumbres Observatory Global Telescope Network Incorporated, the National Central University of Taiwan, the Space Telescope Science Institute, the National Aeronautics and Space Administration under grant No. NNX08AR22G issued through the

Planetary Science Division of the NASA Science Mission Directorate, National Science Foundation grant No. AST-1238877, the University of Maryland, Eotvos Lorand University (ELTE), the Los Alamos National Laboratory, and the Gordon and Betty Moore Foundation.

This publication makes use of data products from the Wide-field Infrared Survey Explorer, which is a joint project of the University of California, Los Angeles, and the Jet Propulsion Laboratory/California Institute of Technology, funded by the National Aeronautics and Space Administration.

This work has made use of data from the European Space Agency (ESA) mission Gaia (<https://www.cosmos.esa.int/gaia>), processed by the Gaia Data Processing and Analysis Consortium (DPAC; <https://www.cosmos.esa.int/web/gaia/dpac/consortium>). Funding for the DPAC has been provided by national institutions, in particular the institutions participating in the Gaia Multilateral Agreement.

The Guoshoujing Telescope (the Large Sky Area Multi-object Fiber Spectroscopic Telescope, LAMOST) is a National Major Scientific Project built by the Chinese Academy of Sciences. Funding for the project has been provided by the National Development and Reform Commission. LAMOST is operated and managed by the National Astronomical Observatories, Chinese Academy of Sciences.

Funding for the Sloan Digital Sky Survey IV has been provided by the Alfred P. Sloan Foundation, the U.S. Department of Energy Office of Science, and the Participating Institutions. The SDSS-IV acknowledges support and resources from the Center for High-Performance Computing at the University of Utah. The SDSS website is www.sdss.org. The SDSS-IV is managed by the Astrophysical Research Consortium for the Participating Institutions of the SDSS Collaboration, including the Brazilian Participation Group, the Carnegie Institution for Science, Carnegie Mellon University, the Chilean Participation Group, the French Participation Group, Harvard-Smithsonian Center for Astrophysics, Instituto de Astrofísica de Canarias, The Johns Hopkins University, the Kavli Institute for the Physics and Mathematics of the Universe (IPMU)/University of Tokyo, the Korean Participation Group, Lawrence Berkeley National Laboratory, Leibniz Institut für Astrophysik Potsdam (AIP), Max-Planck-Institut für Astronomie (MPIA Heidelberg), Max-Planck-Institut für Astrophysik (MPA Garching), Max-Planck-Institut für Extraterrestrische Physik (MPE), the National Astronomical Observatories of China, New Mexico State University, New York University, the University of Notre Dame, Observatório Nacional/MCTI, The Ohio State University, Pennsylvania State University, Shanghai Astronomical Observatory, the United Kingdom Participation Group, Universidad Nacional Autónoma de México, the University of Arizona, the University of Colorado Boulder, the University of Oxford, the University of Portsmouth, the University of Utah, the University of Virginia, the University of Washington, the University of Wisconsin, Vanderbilt University, and Yale University.

Software: astropy (Astropy Collaboration et al. 2013; Price-Whelan et al. 2018), dustmaps (Green 2018), GNU Parallel (Tange 2011), healpy (Zonca et al. 2019), HEALPix (Górski et al. 2005), optuna (Akiba et al. 2019), scikit-learn (Pedregosa et al. 2011), TOPCAT (Taylor et al. 2005), XGBoost (Chen & Guestrin 2016).

ORCID iDs

- Yuming Fu <https://orcid.org/0000-0002-0759-0504>
 Xue-Bing Wu <https://orcid.org/0000-0002-7350-6913>
 Anthony G. A. Brown <https://orcid.org/0000-0002-7419-9679>

References

- Acero, F., Ackermann, M., Ajello, M., et al. 2015, *ApJS*, 218, 23
 Aguado, D. S., Ahumada, R., Almeida, A., et al. 2019, *ApJS*, 240, 23
 Akiba, T., Sano, S., Yanase, T., Ohta, T., & Koyama, M. 2019, in Proc. 25th ACM SIGKDD Int. Conf. on Knowledge Discovery Data Mining (New York: Association for Computing Machinery), 2623
 Andre, P., Ward-Thompson, D., & Barsony, M. 1993, *ApJ*, 406, 122
 Arenou, F., Luri, X., Babusiaux, C., et al. 2018, *A&A*, 616, A17
 Argyriou, A., Evgeniou, T., & Pontil, M. 2006, in Proc. 19th Int. Conf. on Neural Information Processing Systems, ed. B. Schölkopf et al. (Cambridge, MA: MIT Press), 41
 Assef, R. J., Stern, D., Noiro, G., et al. 2018, *ApJS*, 234, 23
 Astropy Collaboration, Robitaille, T. P., Tollerud, E. J., et al. 2013, *A&A*, 558, A33
 Babbedge, T. S. R., Rowan-Robinson, M., Gonzalez-Solares, E., et al. 2004, *MNRAS*, 353, 654
 Bachchan, R. K., Hobbs, D., & Lindegren, L. 2016, *A&A*, 589, A71
 Bailer-Jones, C. A. L., Fouesneau, M., & Andrae, R. 2019, *MNRAS*, 490, 5615
 Becker, R. H., White, R. L., Gregg, M. D., et al. 2001, *ApJS*, 135, 227
 Ben Bekhti, N., Richter, P., Westmeier, T., & Murphy, M. T. 2008, *A&A*, 487, 583
 Ben Bekhti, N., Winkel, B., Richter, P., et al. 2012, *A&A*, 542, A110
 Bishop, C. M. 2006, Pattern Recognition and Machine Learning (Berlin: Springer)
 Blanton, M. R., Bershady, M. A., Abolfathi, B., et al. 2017, *AJ*, 154, 28
 Blitzer, J., McDonald, R., & Pereira, F. 2006, in Proc. 2006 Conf. on Empirical Methods in Natural Language Processing, ed. E. Gaussier & D. Jurafsky (Stroudsburg, PA: Association for Computational Linguistics), 120
 Bovy, J., Hennawi, J. F., Hogg, D. W., et al. 2011, *ApJ*, 729, 141
 Bovy, J., Myers, A. D., Hennawi, J. F., et al. 2012, *ApJ*, 749, 41
 Boyd, K., Eng, K. H., & Page, C. D. 2013, in Joint European Conf. on Machine Learning and Knowledge Discovery in Databases, ed. H. Blockeel et al. (Berlin: Springer), 451
 Brescia, M., Cavaudi, S., D'Abrusco, R., Longo, G., & Mercurio, A. 2013, *ApJ*, 772, 140
 Budavári, T., Csabai, I., Szalay, A. E. S., et al. 2001, *AJ*, 122, 1163
 Chambers, K. C., Magnier, E. A., Metcalfe, N., et al. 2016, arXiv:1612.05560
 Chen, T., & Guestrin, C. 2016, in Proc. 22nd ACM SIGKDD Int. Conf. on Knowledge Discovery and Data Mining (New York: Association for Computing Machinery), 785
 Chicco, D., & Jurman, G. 2020, *BMC Genom.*, 21, 6
 Chiu, K., Fan, X., Leggett, S. K., et al. 2006, *AJ*, 131, 2722
 Condon, J. J., Cotton, W., Greisen, E., et al. 1998, *AJ*, 115, 1693
 Croom, S. M., Richards, G. T., Shanks, T., et al. 2009, *MNRAS*, 392, 19
 Cui, X.-Q., Zhao, Y.-H., Chu, Y.-Q., et al. 2012, *RAA*, 12, 1197
 Davis, J., & Goadrich, M. 2006, in Proc. 23rd Int. Conf. on Machine Learning (New York: Association for Computing Machinery), 233
 Deng, L.-C., Newberg, H. J., Liu, C., et al. 2012, *RAA*, 12, 735
 Dobrzycki, A., Macri, L. M., Stanek, K. Z., & Groot, P. J. 2003, *AJ*, 125, 1330
 Du Plessis, M. C., & Sugiyama, M. 2014, *NN*, 50, 110
 Fan, X., Narayanam, V. K., Lupton, R. H., et al. 2001, *AJ*, 122, 2833
 Farrow, D. J., Cole, S., Metcalfe, N., et al. 2014, *MNRAS*, 437, 748
 Fischer, T. C., Rigby, J. R., Mahler, G., et al. 2019, *ApJ*, 875, 102
 Flesch, E. W. 2015, *PASA*, 32, e010
 Flesch, E. W. 2019, arXiv:1912.05614
 Friedman, J., Hastie, T., Tibshirani, R., et al. 2000, *AnSta*, 28, 337
 Friedman, J. H. 2001, *AnSta*, 29, 1189
 Gaia Collaboration, Brown, A. G. A., Vallenari, A., et al. 2018a, *A&A*, 616, A1
 Gaia Collaboration, Mignard, F., Klioner, S. A., et al. 2018b, *A&A*, 616, A14
 Gaia Collaboration, Prusti, T., De Bruijne, J., et al. 2016, *A&A*, 595, A1
 Glikman, E., Helfand, D. J., & White, R. L. 2006, *ApJ*, 640, 579
 Gong, Z., Zhong, P., & Hu, W. 2019, *IEEE Access*, 7, 64323
 Górski, K. M., Hivon, E., Banday, A. J., et al. 2005, *ApJ*, 622, 759
 Grazian, A., Cristiani, S., D'Odorico, V., Omizzolo, A., & Pizzella, A. 2000, *AJ*, 119, 2540

- Green, G. 2018, *JOSS*, **3**, 695
- Green, G. M., Schlafly, E., Zucker, C., Speagle, J. S., & Finkbeiner, D. 2019, *ApJ*, **887**, 93
- Green, G. M., Schlafly, E. F., Finkbeiner, D., et al. 2018, *MNRAS*, **478**, 651
- Green, R. F., Schmidt, M., & Liebert, J. 1986, *ApJS*, **61**, 305
- Gregg, M. D., Becker, R. H., White, R. L., et al. 1996, *AJ*, **112**, 407
- Hastie, T., Tibshirani, R., & Friedman, J. 2009, *The Elements of Statistical Learning: Data Mining, Inference, and Prediction* (New York: Springer Science+Business Media)
- Hernán-Caballero, A., Hatziminaoglou, E., Alonso-Herrero, A., & Mateos, S. 2016, *MNRAS*, **463**, 2064
- Huo, Z.-Y., Liu, X.-W., Xiang, M.-S., et al. 2013, *AJ*, **145**, 159
- Huo, Z.-Y., Liu, X.-W., Xiang, M.-S., et al. 2015, *RAA*, **15**, 1438
- Huo, Z.-Y., Liu, X.-W., Yuan, H.-B., et al. 2010, *RAA*, **10**, 612
- Im, M., Lee, I., Cho, Y., et al. 2007, *ApJ*, **664**, 64
- Ivezić, Ž., Smith, J. A., Miknaitis, G., et al. 2007, *AJ*, **134**, 973
- Jin, X., Zhang, Y., Zhang, J., et al. 2019, *MNRAS*, **485**, 4539
- Kirkpatrick, J. D., Henry, T. J., & Irwin, M. J. 1997, *AJ*, **113**, 1421
- Koenig, X. P., & Leisawitz, D. T. 2014, *ApJ*, **791**, 131
- Kozłowski, S., & Kochanek, C. S. 2009, *ApJ*, **701**, 508
- Kron, R. G. 1980, *ApJS*, **43**, 305
- Lacy, M., Storrie-Lombardi, L. J., Sajina, A., et al. 2004, *ApJS*, **154**, 166
- Lada, C. J. 1987, in *IAU Symp. 115, Star-forming Regions*, ed. M. Peimbert & J. Jugaku (Cambridge: Cambridge Univ. Press), 1
- Laurino, O., D'Abrusco, R., Longo, G., & Riccio, G. 2011, *MNRAS*, **418**, 2165
- Lindegren, L., Hernández, J., Bombrun, A., et al. 2018a, *A&A*, **616**, A2
- Lindegren, L., Hernández, J., Bombrun, A., et al. 2018b, *IAU 30th General Assembly*, https://www.cosmos.esa.int/documents/29201/1770596/Lindegren_GaiaDR2_Astrometry_extended.pdf
- Luo, A. L., Zhang, H.-T., Zhao, Y.-H., et al. 2012, *RAA*, **12**, 1243
- Luo, A.-L., Zhao, Y.-H., Zhao, G., et al. 2015, *RAA*, **15**, 1095
- Lyke, B. W., Higley, A. N., McLane, J. N., et al. 2020, *ApJS*, **250**, 8
- Magnier, E. A., Schlafly, E. F., Finkbeiner, D. P., et al. 2020, *ApJS*, **251**, 6
- Mainzer, A., Bauer, J., Grav, T., et al. 2011, *ApJ*, **731**, 53
- Mateos, S., Alonso-Herrero, A., Carrera, F. J., et al. 2012, *MNRAS*, **426**, 3271
- Mirabal, N., Charles, E., Ferrara, E. C., et al. 2016, *ApJ*, **825**, 69
- Palanque-Delabrouille, N., Yéche, C., Myers, A. D., et al. 2011, *A&A*, **530**, A122
- Pan, S. J., & Yang, Q. 2009, *IEEE Trans. Knowl. Data Eng.*, **22**, 1345
- Páris, I., Petitjean, P., Aubourg, É., et al. 2018, *A&A*, **613**, A51
- Pasquet-Itam, J., & Pasquet, J. 2018, *A&A*, **611**, A97
- Pedregosa, F., Varoquaux, G., Gramfort, A., et al. 2011, *J. Mach. Learn. Res.*, **12**, 2825
- Planck Collaboration, Abergel, A., Ade, P. A. R., et al. 2014, *A&A*, **571**, A11
- Pounds, K. A. 1979, *RSPSA*, **366**, 375
- Price-Whelan, A. M., Sipőcz, B. M., Günther, H. M., et al. 2018, *AJ*, **156**, 123
- Provost, F., Fawcett, T., & Kohavi, R. 1998, in *Proc. 15th Int. Conf. on Machine Learning*, ed. J. W. Shavlik (Burlington, MA: Morgan Kaufmann), 445
- Quionero-Candela, J., Sugiyama, M., Schwaighofer, A., & Lawrence, N. D. 2009, *Dataset Shift in Machine Learning* (Cambridge, MA: MIT Press)
- Richards, G. T., Fan, X., Newberg, H. J., et al. 2002, *AJ*, **123**, 2945
- Richards, G. T., Nichol, R. C., Gray, A. G., et al. 2004, *ApJS*, **155**, 257
- Richards, G. T., Weinstein, M. A., Schneider, D. P., et al. 2001, *AJ*, **122**, 1151
- Saerens, M., Latrine, P., & Decaestecker, C. 2002, *Neural Comput.*, **14**, 21
- Saito, T., & Rehmsmeier, M. 2015, *PLoS ONE*, **10**, e0118432
- Salvato, M., Hasinger, G., Ilbert, O., et al. 2009, *ApJ*, **690**, 1250
- Sandage, A. 1965, *ApJ*, **141**, 1560
- Savage, B. D., Lu, L., Bahcall, J. N., et al. 1993, *ApJ*, **413**, 116
- Savage, B. D., Wakker, B., Januzzi, B. T., et al. 2000, *ApJS*, **129**, 563
- Schlafly, E. F., Meissner, A. M., Stutz, A. M., et al. 2016, *ApJ*, **821**, 78
- Schmidt, M. 1963, *Natur*, **197**, 1040
- Secrest, N. J., Dudik, R. P., Dorland, B. N., et al. 2015, *ApJS*, **221**, 12
- Shen, S.-Y., Argudo-Fernández, M., Chen, L., et al. 2016, *RAA*, **16**, 43
- Shimodaira, H. 2000, *J. Stat. Plan. Inference*, **90**, 227
- Skrutskie, M., Cutri, R., Stiening, R., et al. 2006, *AJ*, **131**, 1163
- Stern, D., Assef, R. J., Benford, D. J., et al. 2012, *ApJ*, **753**, 30
- Stern, D., Eisenhardt, P., Gorjian, V., et al. 2005, *ApJ*, **631**, 163
- Strauss, M. A., Weinberg, D. H., Lupton, R. H., et al. 2002, *AJ*, **124**, 1810
- Su, D.-Q., & Cui, X.-Q. 2004, *ChJAA*, **4**, 1
- Sugiyama, M., & Kawanabe, M. 2012, *Machine Learning in Non-stationary Environments: Introduction to Covariate Shift Adaptation* (Cambridge, MA: MIT Press)
- Tange, O. 2011, *GNU Parallel 2018*, Zenodo, <https://doi.org/10.5281/zenodo.1146014>
- Taylor, M. B. 2005, in *ASP Conf. Ser. 347, Astronomical Data Analysis Software and Systems XIV*, ed. P. Shopbell, M. Britton, & R. Ebert (San Francisco, CA: ASP), 29
- Vanden Berk, D. E., Richards, G. T., Bauer, A., et al. 2001, *AJ*, **122**, 549
- Vapnik, V. 2013, *The Nature of Statistical Learning Theory* (New York: Springer Science+Business Media)
- Vennes, S., Smith, R. J., Boyle, B. J., et al. 2002, *MNRAS*, **335**, 673
- Wang, S., & Chen, X. 2019, *ApJ*, **877**, 116
- Wang, S.-g., Su, D.-q., Chu, Y.-q., Cui, X., & Wang, Y.-n. 1996, *ApOpt*, **35**, 5155
- Weinstein, M. A., Richards, G. T., Schneider, D. P., et al. 2004, *ApJS*, **155**, 243
- Wenger, M., Ochseneben, F., Egret, D., et al. 2000, *A&AS*, **143**, 9
- Westmeier, T. 2018, *MNRAS*, **474**, 289
- White, R. L., Becker, R. H., Gregg, M. D., et al. 2000, *ApJS*, **126**, 133
- Wright, E. L., Eisenhardt, P. R., Mainzer, A. K., et al. 2010, *AJ*, **140**, 1868
- Wu, X.-B., Hao, G., Jia, Z., Zhang, Y., & Peng, N. 2012, *AJ*, **144**, 49
- Wu, X.-B., & Jia, Z. 2010, *MNRAS*, **406**, 1583
- Wu, X.-B., Zhang, W., & Zhou, X. 2004, *ChJAA*, **4**, 17
- Yan, L., Donoso, E., Tsai, C.-W., et al. 2013, *AJ*, **145**, 55
- Yang, Q., Wu, X.-B., Fan, X., et al. 2017, *AJ*, **154**, 269
- Yao, S., Wu, X.-B., Ai, Y. L., et al. 2019, *ApJS*, **240**, 6
- Yéche, C., Petitjean, P., Rich, J., et al. 2010, *A&A*, **523**, A14
- Yi, Z., Chen, Z., Pan, J., et al. 2019, *ApJ*, **887**, 241
- York, D. G., Adelman, J., Anderson, J. E., Jr., et al. 2000, *AJ*, **120**, 1579
- Yuan, H.-B., Liu, X.-W., Huo, Z.-Y., et al. 2015, *MNRAS*, **448**, 855
- Zhang, Y., Ma, H., Peng, N., Zhao, Y., & Wu, X.-b. 2013, *AJ*, **146**, 22
- Zhao, G., Zhao, Y.-H., Chu, Y.-Q., Jing, Y.-P., & Deng, L.-C. 2012, *RAA*, **12**, 723
- Zonca, A., Singer, L., Lenz, D., et al. 2019, *JOSS*, **4**, 1298